Fermilab FERMILAB-THESIS-1997-27

Search for $D^0 - \overline{D}^0$ Mixing Using Semileptonic Decays

DISSERTATION

Presented in Partial Fulfillment of the Requirements for
the Degree of Doctor of Philosophy in the Graduate
School of The Ohio State University

By
Arun K. Tripathi, M.Sc.

* * * * * * * * * *

The Ohio State University

1997

Dissertation Committee:
Professor N. W. Reay, Adviser
Professor N. R. Stanton
Professor J. Shigemitsu

Approved By:

Adviser
Physics Graduate Program

ABSTRACT

The analysis presented in this thesis is the first search for $D^0 - \overline{D}^0$ mixing using reconstructed semileptonic decays. In the Standard Model, the rate of $D^0 - \overline{D}^0$ mixing is expected to be several orders of magnitude below the current experimental sensitivity. However, there are physics models that predict large $D^0 - \overline{D}^0$ mixing at levels accessible to existing experiments, and any observation of mixing at the level of current experimental sensitivities would be a clear indication of new physics. Results from previous mixing searches are model-dependent since they involve making certain crucial assumptions. Use of semileptonic decays to search for $D^0 - \overline{D}^0$ mixing eliminates the need to make these assumptions, hence results obtained from this method are model-independent and straightforward to interpret.

Data from Fermilab hadroproduction experiment E791 were used for this analysis. The charge of the pion from the strong decay $D^{*+} \rightarrow D^0 \pi^+$ (and charge conjugate) is used to identify the charm quantum number of the neutral D at production, and the charge of the lepton and the kaon in semileptonic decays $D^0 \rightarrow Ke\nu$ and $K\mu\nu$ is used to identify the charm at the time of decay. No evidence of mixing is seen, and a 90% confidence level upper limit on mixing of $r < 0.50\%$ is obtained, where $r =$, $(D^0 \rightarrow \overline{D}^0 \rightarrow K^+ l^- \bar{\nu}_l)/$, $(D^0 \rightarrow K^- l^+ \nu_l)$. This is the best model-independent limit on $D^0 - \overline{D}^0$ mixing to date.

Dedicated To Mother and Father

ACKNOWLEDGMENTS

First of all, I wish to thank my adviser Bill Reay for suggesting an interesting thesis topic, helping me with the analysis, and guiding me through various steps in the world of high energy physics. I met him on my day 2 in USA, and he has always been a source of encouragement, enthusiasm, help and good advice (in and outside physics) since then. His accurate and positive criticism and continuous feedback have been extremely valuable to me. I thank Noel Stanton for taking an active interest in and carefully reviewing my analysis, suggesting improvements, and helping me write the paper. He was always encouraging and very patient while answering my questions. Thanks to Ron Sidwell for his help in my understanding of the E791 experiment in detail and in getting me started on various analysis techniques. It has been fun working with this wonderful group.

I thank the E791 collaboration for making this experiment and hence this analysis possible. Especially, I would like to thank Pat Burchat and Guy Blaylock for having me over at UC Santa Cruz, and helping me with the analysis and fitting techniques. Thanks also to Jean Slaughter, Jeff Appel, Milind Purohit and Mike Sokoloff for taking interest in my analysis and providing useful suggestions. Thanks to Chong Zhang for his help with the semileptonic monte-carlo generation, and to Jeff Smith for help with computer questions/troubles.

I also want to thank all my friends for making my stay in graduate school and in Columbus, and later in Manhattan (Kansas) fun. List of all of their names would be too long, but I must mention one name. Thank you Lisa, for a wonderful friendship and a lot of help in rough times, especially during the days of my badly broken right leg.

Thanks to Brenda Mellett, the graduate studies secretary at OSU, who was always very friendly and helpful, even when I used to call her up from Kansas (after the group moved to KSU) and bother her with all kinds of questions and requests for help. Thanks also to Ann Belair and Elizabeth Smith for patiently making arrangements for me to get paid from Ohio State University, even after the group moved to Kansas State.

Special thanks to my american host family, Lu and Bob Mone, for all those thanksgiving, Christmas and 4th of July dinners, and the birthday cakes, and all the postcards and letters that I still keep getting from them even after moving to Kansas.

VITA

November 18, 1969 ..... Born - Chunar, India

May 1990 ..... M.S. Physics

Indian Institute of Technology,

Kanpur, India.

June 1990 ..... Graduate Teaching Assistant

The Ohio State University

January 1992 ..... Graduate Research Assistant

The Ohio State University

December 1992 ..... M.S., Physics

The Ohio State University

PUBLICATIONS

1. E791 Collaboration, E. M. Aitala *et al.*, "Search for $D^0\bar{D}^0$ Mixing in Semileptonic Decay Modes." Phys. Rev. Lett **77**, 2384 (1996).

2. E791 Collaboration, E. M. Aitala *et al.*, "Mass Splitting and Production of Σ_c^0 and Σ_C^{++} Measured in 500 GeV π^--N Interactions." Phys. Lett. **B379**, 292 (1996).

3. E791 Collaboration, E. M. Aitala *et al.*, "Asymmetries between the Production of

D^+ and D^- Mesons from 500-GeV/c π^- Nucleon Interactions as a Function of x_f and P_T^2." Phys. Lett. **B371**, 157 (1996).

4. E791 Collaboration, E. M. Aitala *et al.*, "Search for Flavor Changing Neutral Current Decays $D^+ \to \pi^+\mu^+\mu^-$ and $D^+ \to \pi^+e^+e^-$." Phys. Rev. Lett. **76**, 364 (1995).

FIELDS OF STUDY

Major Field: Elementary Particle Physics

Table of Contents

Abstract ii

Vita vi

1 Theory and Motivation **1**

1.1 Introduction 1

1.2 $D^0 - \overline{D}^0$ Mixing in the Standard Model 2

1.2.1 Short-Range Contribution 2

1.2.2 Long-Range Effects 3

1.3 Extensions of the Standard Model with Large Mixing 4

1.3.1 Flavor-Changing Neutral Higgs 5

1.3.2 A Fourth-Generation b-Type Quark 6

1.3.3 Scalar Leptoquarks 6

1.3.4 Supersymmetric Models 7

1.3.5 Multiscalar Models with Natural Flavor Conservation 7

1.4 Experimental Signature of Mixing 7

1.4.1 Implications of a Mixing Search using Hadronic Decays of the D^0 . 9

1.4.2 Mixing Search Using Semileptonic Decays 9

1.5 Time Evolution of Mixing and CP Issues 10

1.6 Experimental Motivation for Mixing Search Using Semileptonic Decays . . . 15

2 The E791 Experimental Setup 17

2.1 Introduction 17

2.2 Beamline 17

2.3 Target 18

2.4 E791 Spectrometer 19

2.5 E791 Coordinate System 21

2.6 Beam Tracking 22

2.7 Vertex Reconstruction – Silicon Microstrip Detectors 22

2.8 Downstream Tracking – Drift Chambers and PWC's 23

2.9 Momentum and Charge Measurement – Magnets 26

2.10 Particle Identification 26

2.10.1 Čerenkov Detectors 26

2.10.2 Segmented Liquid Ionization Calorimeter (SLIC) 29

2.10.3 Hadronic Calorimeter 30

2.10.4 Muon Identification 32

2.11 Trigger and Data Acquisition System 33

3 Data Reconstruction and Event Selection 43

3.1 Introduction 43

3.2 Event Reconstruction and Filtering 43

3.2.1 Track and Vertex Reconstruction 45

3.2.2 Particle Identification 45

3.2.3 Filtering 46

3.3 Further Data Reduction 46

3.4 Final Particle Identification Criteria 47

3.4.1 Kaon Identification 48

3.4.2 Electron Identification 48

3.4.3 Muon Identification 49

3.5 Final Selection Criteria 51

3.5.1 The Selection Criteria Common to $Ke\nu$ and $K\mu\nu$ Modes 51

3.5.2 Cuts Used in $Ke\nu$ Analysis Only 58

3.5.3 Cuts Used in $K\mu\nu$ Analysis Only 58

4 The Analysis and Fitting Technique 60

4.1 Introduction 60

4.2 Calculation of Q and t 60

4.3 Maximum Likelihood Fit 62

4.3.1 Likelihood Function 62

4.4 Fit Results 71

4.5 The Relative Correction Factor, α 73

4.6 Calculation of the Mixing Rate 77

4.6.1 Combined Mixing Rate From the Two Modes 77

4.7 Some Systematic Checks 78

4.7.1 Effect of Hadronic Feedthrough 80

4.7.2 Effect of Smearing in Signal Decay-Time Distribution 82

4.7.3 Test of the Sensitivity of the Fit to a Small Mixing Signal 89

4.7.4 Test of the Method to Calculate α 90

4.7.5 Check for Bias in α due to the Choice of Neutrino Momentum . . . 91

4.7.6 Summary of Systematic Checks 91

5 Final Results and Conclusion 94

5.1 Introduction 94

5.2 Final Results 94

5.3 A Survey of Previous $D^0 - \overline{D}^0$ Mixing Measurements 95

5.3.1 Fermilab E691 95

5.3.2 Fermilab E615 96

5.3.3 CLEO II 96

5.3.4 Fermilab E791, Hadronic Analysis 97

5.4 Conclusion 98

A An Estimate and Parametrization of D^* Mass Resolution 103

B Some Details of Muon Identification 109

B.1 Calculation of MUCAT 109

B.2 Use of TDC Information in Y Muon Wall 109

List of Figures

1.1 Box diagrams for $D^0 - \overline{D}^0$ mixing. 3

1.2 A Feynman diagram for long-range contributions to $D^0 - \overline{D}^0$ mixing . . . 4

1.3 A Feynman diagram for mixing via tree level Flavor Changing Neutral Currents. 5

1.4 A box diagram for Flavor Changing Neutral Higgs contribution to $D^0 - \overline{D}^0$ mixing. 5

1.5 A Feynman diagram for $D^0 - \overline{D}^0$ mixing with a heavy fourth generation b' quark. 6

1.6 A Feynman diagram showing the leptoquark contribution to $D^0 - \overline{D}^0$ mixing. 7

1.7 Feynman diagram for the decay $D^0 \to K^-\pi^+$. 9

1.8 Feynman diagram for the doubly-Cabibbo-suppressed decay $D^0 \to K^+\pi^-$. 10

1.9 Feynman diagram for the semileptonic decay $D^0 \to K^-l^+\nu_l$. 10

1.10 An example of possible decay-time distributions of mixing, DCS and the interference terms. 14

2.1 Layout of the Fermilab beam lines 18

2.2 The schematic layout of the E791 target foils. 19

2.3 The E791 Spectrometer 20

2.4 The E791 coordinate system. 21

2.5 The schematic of upstream PWC-SMD system to track the beam. 22

2.6 Schematic of the first Čerenkov detector, C1. 36

2.7 Schematic of the second Čerenkov detector, C2. 36

2.8 Schematic of the mirror segmentation in C1 and C2 Čerenkov detectors. . . 37

2.9 The schematic view of the SLIC. 38

2.10 Side view of the muon system. 38

2.11 Top view of the muon system. 39

2.12 The geometry of the X muon wall. 40

2.13 Geometry of the Y muon wall. 41

2.14 Location of scintillating paddles used in trigger decision. 41

2.15 Schematic of the DA system used in E791. 42

3.1 Flow chart outlining the process of data reduction. 44

3.2 A schematic of the D^*-D^0 decay chain topology. 47

3.3 Q-value distributions for Monte Carlo $Ke\nu$ and $K\mu\nu$ signals. 52

3.4 M_{min} distributions for signal and background. 53

3.5 M_{Kl} distribution for signal and background events. 54

3.6 Mass spectrum of the $K - l$ vertices when the lepton is assigned the π mass. 55

3.7 P_T^l distribution for signal and background events. 56

3.8 P_T^h distribution for signal and background events. 57

3.9 M_{min}^{ee} distributions for MC $Ke\nu$ signal and data background. 58

4.1 Q-value distributions for $Ke\nu$ and $K\mu\nu$ modes after final cuts. 63

4.2 Q-value distribution for the $Ke\nu$ mode in different decay-time bins. 66

4.3 Q-value distribution for the $K\mu\nu$ mode in different decay-time bins. 67

4.4 Signal and background decay-time distributions for $Ke\nu$ and $K\mu\nu$ samples. 70

4.5 Background decay-time distributions for right- and wrong-sign events. . . . 71

4.6 Decay time distributions for the events in various Q-value regions. 72

4.7 The projections of the fit onto Q-value distributions. 74

4.8 Distributions of the correction factor α 76

4.9 The decay time distribution of the wrong-sign events in the signal region. . 79

4.10 Smearing distributions in different time bins for the $Ke\nu$ mode. 83

4.11 Smearing distributions in different time bins for the $K\mu\nu$ mode. 84

4.12 True decay-time distributions for the $Ke\nu$ and $K\mu\nu$ MC events. 85

4.13 Simulated exponential and mixed decay-time distributions for the $Ke\nu$ and $K\mu\nu$ modes. 86

A.1 Schematic of semileptonic decay topology 104

B.1 Scatter plot of Y-wall TDC counts vs. projected X position on Y muon wall. 112

List of Tables

2.1 Characteristics of the E791 SMD system. 24

2.2 Characteristics of the E791 PWC systems. 25

2.3 Characteristics of the E791 drift chambers. 25

2.4 The characteristics of the E791 Čerenkov detectors 27

2.5 Čerenkov Separation for π, K and p 28

2.6 Mirror sizes in one quarter of the Čerenkov mirror plane in C1 and C2. . . 29

2.7 Important Characteristics of the SLIC. 31

2.8 Characteristics of the X and Y muon walls 34

4.1 Results from the maximum likelihood fit to the data 73

4.2 Effect of smearing in decay time on N_{mix}. 88

4.3 Results of various fits to MC samples with known amounts of mixing. . . . 90

4.4 Results of the fit when a known fixed number of mixed MC events were added to WS data. 92

4.5 Test of the method used to calculate α. 93

4.6 Values of α from Monte Carlo using true and measured proper decay-time. 93

B.1 Description of the tagging requirements of a muon candidate for a given value of MUCAT 110

Chapter 1

Theory and Motivation

1.1 Introduction

The Standard Model (SM) has had spectacular success in describing most of the particle physics phenomena observed so far, but there are reasons to believe that there is new physics beyond the SM. For example, the Standard Model has no theory for CP violation, and it also cannot predict masses of the fundamental particles.

One way to look for new physics is to search for processes that are predicted to happen only rarely (or are forbidden) in the Standard Model. If these processes are observed to occur at a rate significantly higher than the predicted rate, it might be an indication of physics beyond the Standard Model. One such process is $D^0 - \overline{D}^0$ mixing.

Mixing is a process in which a particle evolves into its own antiparticle spontaneously, in this case a D^0 evolves into a $\overline{D}^0$. This process is unique to certain neutral mesons, and has been observed only in K^0 and B^0 mesons. In the Standard Model, the $D^0 - \overline{D}^0$ mixing rate is predicted to be far below current experimental sensitivities. However, there are extensions to the Standard Model that allow much larger mixing. Therefore, if mixing is seen by an experiment, it would be an indication of physics beyond the Standard Model. Thus, mixing provides a sensitive probe of the weak interactions, and it is a good ground

for testing the accuracy of the Standard Model.

The mixing rate is parameterized as:

$$r = \frac{,\ (D^0 \ \to \overline{D}^0 \ \to \bar{f})}{,\ (D^0 \ \to f)}. \tag{1.1}$$

where f is the final decay state used to identify the charm quantum number of the neutral D at the time of decay.

In this chapter the predictions for $D^0 - \overline{D}^0$ mixing rate in the Standard Model and also in some new physics models are outlined. Then the signatures of mixing that one looks for and some theoretical issues that arise as a consequence are discussed. Finally, the time evolution of mixing is derived for the most general case and simplified for semileptonic decays.

1.2 $D^0 - \overline{D}^0$ Mixing in the Standard Model

Contributions to $D^0 - \overline{D}^0$ mixing in the Standard Model can be broadly classified into two categories – short-range and long-range, as described below.

1.2.1 Short-Range Contribution

The Feynman diagrams corresponding to the lowest-order short-range box diagram mixing are shown in Figure 1.1.

Ignoring the contribution from b quark (which is suppressed due to a small Cabibbo coupling), the amplitude for the box diagram contribution to mixing is given by [1]:

$$A_{D^0}^{Box} \propto |V_{cs}^* V_{us}|^2 \left(\frac{m_s^2 - m_d^2}{m_W^2} \right) \times \left(\frac{m_s^2 - m_d^2}{m_c^2} \right). \tag{1.2}$$

The box diagram contribution to $D^0 - \overline{D}^0$ mixing is very small due both to nearly complete GIM cancellations, and also to heavy quark suppression (which comes in as

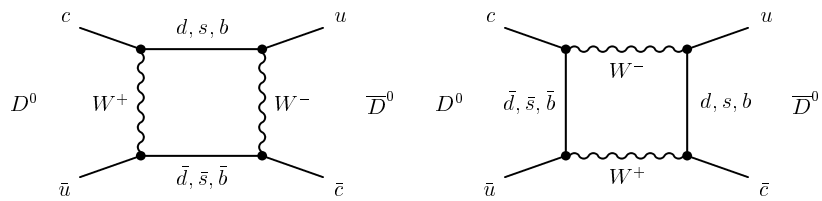

Figure 1.1: Box diagrams for $D^0 - \overline{D}^0$ mixing.

$(m_s^2 - m_d^2)/m_c^2)$ [1]. In the limit of SU(3) symmetry, when the masses of the up (u), down (d) and strange (s) quarks are equal, the mixing rate vanishes. Estimates of this box diagram contribution yield:

$$r_{box} \sim 10^{-10}. \tag{1.3}$$

1.2.2 Long-Range Effects

The box diagram calculation of mixing considers only short-range interactions, treating the quarks as free particles. A larger contribution to charm mixing could come from long-range effects (Figure 1.2) [2, 3, 4, 5] where intermediate states are bound hadrons rather than free quarks. Any intermediate hadronic decay state which couples to both D^0 and $\overline{D}^0$ could contribute to this effect (e.g. $D^0 \rightarrow \pi\pi$, KK, etc.$\rightarrow \overline{D}^0$). The calculation of this contribution is complicated by the nonperturbative strong interactions, which bind quarks into hadrons. Also, there are many cancellations between contributions from different intermediate states. In fact, cancellation is complete in the SU(3) limit, just as in the box diagram case.

It was previously thought that the long-range effects might give rise to mixing rates as large as $r = 10^{-3}$ [2, 3]. However, more recent estimates based on Heavy Quark Effective Theory (HQET) [4, 5] suggest that cancellations are more complete than previously

thought. Enhancement to SM mixing due to long-range effects is expected to be modest, no more than a factor of 10 over the box diagram.

Conservative estimates [6] set an upper limit on Standard Model $D^0 - \overline{D}^0$ mixing of:

$$r_{SM} < 10^{-8}. \tag{1.4}$$

The rate of $D^0 - \overline{D}^0$ mixing in the Standard Model is, therefore, several orders of magnitude below current experimental sensitivities ($\sim 10^{-3}$).

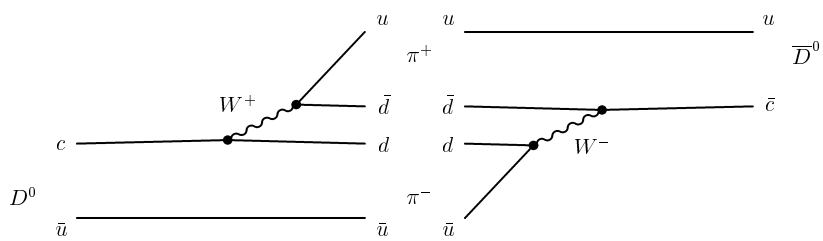

Figure 1.2: A typical Feynman diagram for long-range contributions to $D^0 - \overline{D}^0$ mixing (in this case $D^0 \to \pi^+\pi^- \to \overline{D}^0$).

1.3 Extensions of the Standard Model with Large Mixing

There are various extensions to the Standard Model that allow large $D^0 - \overline{D}^0$ mixing that would be observable by existing experiments. For a review of contributions to $D^0 - \overline{D}^0$ mixing from new physics, see references [6, 7, 8] and references therein. Some of these models are discussed below.

1.3.1 Flavor-Changing Neutral Higgs

Flavor Changing Neutral Currents (FCNC) at the tree level are not allowed in the Standard Model. But there are multi-Higgs models [9, 10, 11]where flavor changing couplings are present, and FCNC could contribute to mixing via tree (Figure 1.3) or box (Figure 1.4) level diagrams with intermediate H^0.

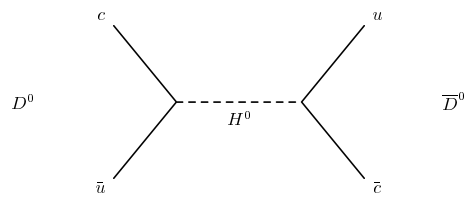

Figure 1.3: A Feynman diagram for mixing via tree level Flavor Changing Neutral Currents.

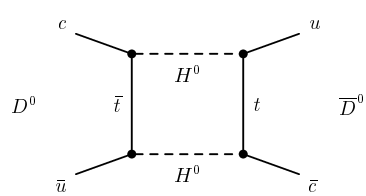

Figure 1.4: A Box digram for FCNC contribution to $D^0 - \overline{D}^0$ mixing. The top quark, which has a very high mass, can participate in the box diagram (if FCNC is allowed), possibly contributing significantly to $D^0 - \overline{D}^0$ mixing.

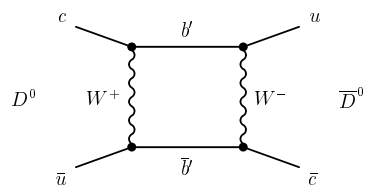

Figure 1.5: A heavy b' quark with -1/3 charge could enhance the short-range $D^0 - \overline{D}^0$ mixing by participating in the box diagram

1.3.2 A Fourth-Generation b-Type Quark

One reason the box diagram short-range contribution to $D^0 - \overline{D}^0$ mixing in the SM is so small is that there are no heavy particles participating in the box diagram to enhance the rate. If there exists a fourth generation b-type quark with -1/3 charge (b') [12], it could contribute significantly to the box diagrams for appropriate values of b' mass and the Cabibbo coupling $V_{cb'}$(Figure 1.5).

The mixing amplitude from this kind of diagram is proportional to [12]:

$$A^{b'}_{Box} \propto |V_{cb'} V^*_{ub'}|^2 F(m^2_{b'}/m^2_W). \tag{1.5}$$

Thus, for large enough b' mass and $|V_{cb'} V^*_{ub'}|$, the contribution to $D^0 - \overline{D}^0$ mixing from this source could be large.

1.3.3 Scalar Leptoquarks

Leptoquarks are naturally present in models [13, 14] that put quarks and leptons on equal footing. They would couple to both leptons and quarks with an unknown coupling constant. The scalar leptoquarks can contribute to $D^0 - \overline{D}^0$ mixing by participating in the box digrams as shown in Figure 1.6.

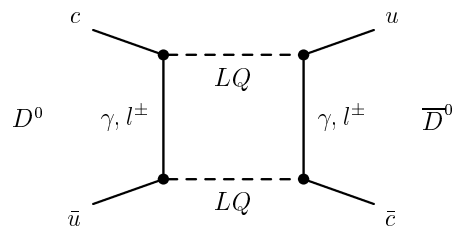

Figure 1.6: A Feynman diagram showing the leptoquark contribution to $D^0 - \overline{D}^0$ mixing.

1.3.4 Supersymmetric Models

In supersymmetric models [15, 16]with quark-squark alignment, $D^0 - \overline{D}^0$ mixing gets contributions from box diagrams with gluinos and squarks. Contributions from this source could possibly be as large as the existing experimental bounds.

1.3.5 Multiscalar Models with Natural Flavor Conservation

In multiscalar models with natural flavor conservation (NFC) [17, 18, 19], mixing gets new contributions from box diagrams with intermediate $H^{\pm}$ and quarks. For appropriate values of the parameters involved, such contributions could be of the order of existing experimental bounds.

1.4 Experimental Signature of Mixing

This section describes the experimental signature of mixing as used in the mixing search, since important theoretical issues arise depending on how one looks for mixing. In order to search for mixing experimentally, one has to identify the charm of the neutral D at the time of production and also at the time of decay. A mismatch between the two could be

a signature of mixing.

The D^* tag is used in this analysis to identify the charm quantum number of the neutral D at the time of production. The charge of the pion from the strong decay $D^{*+} \rightarrow \pi^+ D^0$ identifies the charm quantum number of the neutral D at the time of production, and the decay products of the neutral D are used to identify the charm of the D at the time of decay. If no mixing took place, then the $D^* - D^0$ decay chain would look like:

$$D^{*+} \rightarrow \pi^+ D^0 \rightarrow \pi^+ (K^- X) \tag{1.6}$$

In the above decay chain, X could be purely hadronic (*e.g.* π^+) or semileptonic (*e.g.* $l^+ \nu_l$). Note that in this decay chain, the charge of the kaon from the decay of the neutral D is *opposite* to the charge of the pion from the D^* decay. These decays are Cabibbo-allowed and are referred to as *right-sign* (RS) decays.

If mixing took place, then the decay chain would look like:

$$D^{*+} \rightarrow \pi^+ D^0 \rightarrow \pi^+ \overline{D}^0 \rightarrow \pi^+ (K^+ \overline{X}). \tag{1.7}$$

In the above decay chain, a particle that was produced as a D^0 oscillated into a $\overline{D}^0$ before it decayed. Note that in this decay chain, the charge of the kaon from the decay of the neutral D is the *same* as that of the pion from the D^* decay. These decays are also known as *wrong-sign* (WS) decays, and this is the signature of mixing looked for by E791.

An added advantage of using the D^* tag is that it provides a very narrow and clean signal, thus reducing background. The amount of phase space available in the decay $D^{*+} \rightarrow \pi^+ D^0$ is very small ($M(D^{*+}) - M(D^0) - M(\pi) = 5.8$ MeV/c^2), resulting in a narrow peak in the mass difference.

1.4.1 Implications of a Mixing Search using Hadronic Decays of the D^0

Purely hadronic decays of D^0 have previously been used in mixing searches to identify the charm of the neutral D at the time of decay. The full D^0 momentum is measured in these decays, resulting in clean and narrow D^* signals. However, in hadronic decay modes, doubly-Cabibbo-suppressed (DCS) decays also can give rise to a wrong-sign signal without any mixing. For example, Figure 1.8 shows the Feynman diagram for the DCS decay $D^0 \rightarrow K^+ \pi^-$. Although the DCS decay rate is expected to be small, of the order $tan^4\theta_c$ times the Cabibbo allowed rate, it is a large background for a rare process such as mixing. The DCS amplitude can also interfere with the mixing amplitude, further masking a mixing signal. Although the proper decay time distribution can be used to statistically separate mixing, DCS and interference terms (see section 1.5), this requires extra fitting parameters which reduce the sensitivity.

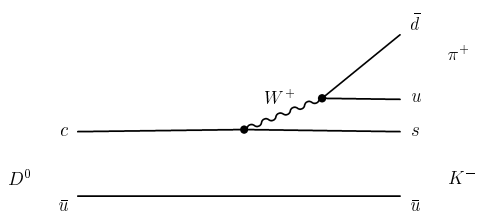

Figure 1.7: Feynman diagram for the decay $D^0 \rightarrow K^-\pi^+$.

1.4.2 Mixing Search Using Semileptonic Decays

Semileptonic decays have no DCS amplitude. This eliminates the problem of interference between mixing and DCS amplitudes, and simplifies the interpretation of any wrong-sign signal. Any observation of a wrong-sign signal in semileptonic decays with the mixing

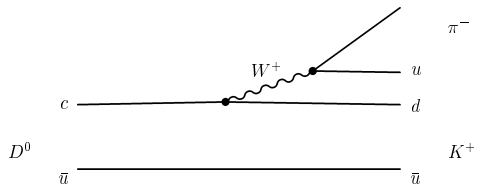

Figure 1.8: Feynman diagram for the doubly-Cabibbo-suppressed decay $D^0 \to K^+\pi^-$.

decay time distribution (described in section 1.5) becomes clear evidence for mixing. The Feynman diagram for the semileptonic decay $D^0 \to K^-l^+\nu_l$ is shown in Figure 1.9.

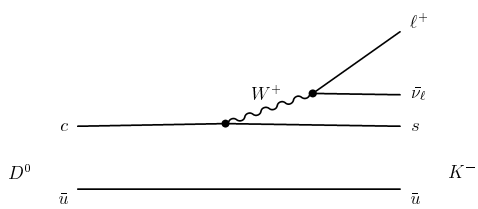

Figure 1.9: Feynman diagram for the semileptonic decay $D^0 \to K^-l^+\nu_l$.

1.5 Time Evolution of Mixing and CP Issues

In this section, the most general expression for the time evolution of mixing is derived, and a simplified formula is extracted for semileptonic decays.

In mixing, a particle produced as a D^0 at time $t = 0$ acquires an amplitude to be a $\overline{D}^0$ at subsequent times t. In the most general case, CP is not conserved. Mass eigenstates can be written as:

$$\begin{aligned} |D_1> &= p|D^0> + q|\overline{D}^0> \\ |D_2> &= p|D^0> - q|\overline{D}^0>, \end{aligned} \tag{1.8}$$

with the normalization

$$|p|^2 + |q|^2 = 1. \tag{1.9}$$

The mass eigenstates D_i evolve in time according to:

$$|D_i(t)> = f_i(t)|D_i(t=0)>, \tag{1.10}$$

where

$$f_i(t) = e^{-iM_i t - \frac{1}{2}\Gamma_i t}. \tag{1.11}$$

The mass and width of the physical states are given by M_i and , $_i$ respectively. The time evolution of $|D^0(t)>$, which starts out as a pure $|D^0>$ at t=0 (and charge conjugate equation), is obtained by inverting equations 1.8:

$$\begin{aligned} |D^0(t)> &= \frac{1}{2p}[(p|D^0> + q|\overline{D}^0>)f_1(t) + (p|D^0> - q|\overline{D}^0>)f_2(t)] \\ &= \frac{1}{2}(f_1 + f_2)|D^0> + \frac{q}{2p}(f_1 - f_2)|\overline{D}^0>, \end{aligned} \tag{1.12}$$

and similarly for $\overline{D}^0$. The above equations can be re-written as:

$$
\begin{aligned}
|D^0(t)> &= f_+(t)|D^0> + \frac{q}{p} f_-(t)|\overline{D}^0> \\
|\overline{D}^0(t)> &= \frac{p}{q} f_-(t)|D^0> + f_+(t)|\overline{D}^0>,
\end{aligned} \tag{1.13}
$$

where

$$
\begin{aligned}
f_+(t) &\equiv e^{-iMt-\frac{1}{2}\Gamma t} \cos(\tfrac{1}{2}\Delta M t - \frac{i}{4}\Delta, t) \\
f_-(t) &\equiv e^{-iMt-\frac{1}{2}\Gamma t}\, i \sin(\tfrac{1}{2}\Delta M t - \frac{i}{4}\Delta, t),
\end{aligned} \tag{1.14}
$$

and

$$
\begin{aligned}
M &\equiv \tfrac{1}{2}(M_1 + M_2), \qquad \Delta M \equiv M_2 - M_1 \\
, &\equiv \tfrac{1}{2}(,_1 + ,_2), \qquad \Delta, \equiv ,_2 - ,_1.
\end{aligned} \tag{1.15}
$$

Define a wrong-sign decay as the decay of a state produced as $|D^0>$ into a final state $|\bar{f}>$ characteristic of a $\overline{D}^0$ decay (and the charge conjugate process). In the most general case, the doubly-Cabibbo-suppressed (DCS) amplitude is non-zero, and CP is not necessarily conserved. There are then four different amplitudes for the decay into a wrong-sign final state:

$$
\begin{aligned}
A &\equiv <f|H|D^0>, \qquad B \equiv <f|H|\overline{D}^0> \\
\bar{A} &\equiv <\bar{f}|H|\overline{D}^0>, \qquad \bar{B} \equiv <\bar{f}|H|D^0>.
\end{aligned} \tag{1.16}
$$

A and $\bar{A}$ represent the DCS amplitudes, and B and $\bar{B}$ are the Cabibbo-favored amplitudes. The decay amplitudes into the wrong sign final states are given by:

$$
\begin{aligned}
< f|H|D^{\,0}(t) > &= B\frac{q}{p}[\lambda f_+(t) + f_-(t)] \\
< \bar{f}|H|\overline{D}^{\,0}(t) > &= \bar{B}\frac{p}{q}[f_-(t) + \bar{\lambda} f_+(t)],
\end{aligned} \tag{1.17}
$$

where

$$
\lambda \equiv \frac{pA}{qB}, \qquad \bar{\lambda} \equiv \frac{q\bar{A}}{p\bar{B}}. \tag{1.18}
$$

The decay rates are given by:

$$
\begin{aligned}
, [D^{\,0}(t) \to f] &= |< f|H|D^{\,0}(t) > |^2 \\
, [\overline{D}^{\,0}(t) \to \bar{f}] &= |< \bar{f}|H|\overline{D}^{\,0}(t) > |^2.
\end{aligned} \tag{1.19}
$$

Assuming $\Delta M << \, , \, , \, \Delta, \, << \, ,$ and $|\lambda| << 1$ (as confirmed experimentally), the decay rates can be written as:

$$
, [D^{\,0}(t) \to f] = \frac{e^{-\Gamma t}}{4}|B|^2|\frac{q}{p}|^2 \times [4|\lambda|^2 + (\Delta M^2 + \frac{\Delta, \, ^2}{4})t^2 + 2Re(\lambda)\Delta, \, t + 4Im(\lambda)\Delta M t] \tag{1.20}
$$

$$
, [\overline{D}^{\,0}(t) \to \bar{f}] = \frac{e^{-\Gamma t}}{4}|\bar{B}|^2|\frac{p}{q}|^2 \times [4|\bar{\lambda}|^2 + (\Delta M^2 + \frac{\Delta, \, ^2}{4})t^2 + 2Re(\bar{\lambda})\Delta, \, t + 4Im(\bar{\lambda})\Delta M t] \tag{1.21}
$$

These equations give the most general expression for the decay rate into a wrong-sign final state [20].

If a purely hadronic decay of D^0 is used to study mixing, the DCS amplitude is not zero and it can interfere with the mixing amplitude. The decay-time distribution of the wrong-sign decays is then given by equations 1.20 and 1.21 above. The mixing, DCS, and

interference terms in each equation have different time dependences, graphically displayed in Figure 1.10, and these differences in principle can be used to separate them. However, the sensitivity of the fits weakens considerably from adding additional terms, since they are all unconstrained.

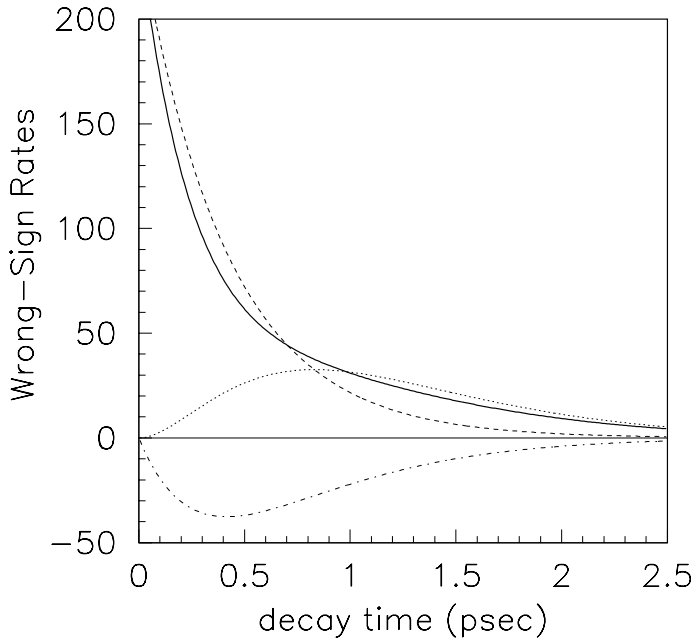

Figure 1.10: An example of possible decay-time distributions of mixing, DCS and the interference terms, taken from [20]. The dashed line represents the DCS contribution. The dotted line shows the contribution due to mixing. The dash-dot line shows the contribution from destructive interference of DCS and mixing amplitudes when the interference is 30% of its maximum. The solid line is the sum of all three contributions.

In the case of semileptonic decays there is no DCS amplitude, implying $A = \bar{A} = \lambda = 0$. Assuming CP is not violated (CP violation in semileptonic decays would arise from direct

CP violation, which is expected to be unlikely), $B = \bar{B}$, and $|q| = |p| = 1/\sqrt{2}$. Decay rates into a wrong-sign final state for D^0 and $\overline{D}^0$ are then identical, and are given by the simplified expression:

$$, [D^0(t) \to f] = \frac{e^{-\Gamma t}}{4}|B|^2[\Delta M^2 + \frac{\Delta,^2}{4}t^2] \tag{1.22}$$

By comparing equation 1.22 with the corresponding equations for hadronic decays (equations 1.20 and 1.21), the simplicity achieved in semileptonic decays is obvious. Integrating equation 1.22 over time and normalizing it to Cabibbo-allowed decays $D^0 \to K^- l^+ \nu_l$, an expression is obtained for the mixing rate:

$$r \equiv \frac{, (D^0 \to \overline{D}^0 \to l^- X)}{, (D^0 \to l^+ X)} = \frac{1}{2}\left[\left(\frac{\Delta M}{,}\right)^2 + \left(\frac{\Delta,}{2,}\right)^2\right] \tag{1.23}$$

It is seen from the above equation that there are two contributions to mixing – one comes from the mass difference, ΔM, between the two CP eigenstates, and the other contribution comes from $\Delta,$, the difference between the decay rates of the two states. In the charm sector, ΔM term is expected to dominate. Due to the large amount of phase space available in charm decays, the difference between the decay rates of the two CP eigenstates is expected to be negligible, i.e., $\Delta, << \Delta M$. This is in contrast with the K^0 sector, where due to the reduced phase space available for the decay of the CP = -1 eigenstate, decay rates of the two CP eigenstates differ greatly.

1.6 Experimental Motivation for Mixing Search Using Semileptonic Decays

The idea of using semileptonic decays of D^0 to search for mixing in a clean (from a physics point of view) and unambiguous manner has been around for a long time, but until now has not been implemented with reconstructed semileptonic decays. The main reason was that semileptonic decays cannot be fully reconstructed, so that the total D^0 momentum cannot

be measured. This results in a wider D^* mass peak with more background compared to purely hadronic decays.

However, a simple analysis (see Appendix A) of the dependence of the D^* mass width on the D^0 momentum reveals that this problem is not as bad as previously thought. The width of the D^* mass peak is not particularly sensitive to the magnitude of the momentum of the D^0, and is limited mainly by the accuracy with which the direction of flight of the D is known. In semileptonic decays, the direction of flight of the D is determined from the displacement vector between the secondary (D^0) and the primary (D^*) vertices. The longer-lived the D^0, more precisely is this vector measured. Since the mixed decays do live longer (mixing peaks at about 2 D^0 lifetimes), the direction of flight of the D^0 is measured with adequate precision for the decays of interest. In addition, the magnitude of the D^0 momentum (and hence proper decay time) can be estimated to approximately 15% accuracy using the vertexing information and the measured momenta of the charged decay products of the D^0. These considerations make it experimentally feasible to search for mixing using semileptonic decays despite the unobserved neutrino.

Chapter 2

The E791 Experimental Setup

2.1 Introduction

The goal of experiment E791 was to explore charm physics with greater sensitivity than previous experiments, which was achieved by collecting a large sample of charm events with an unbiased trigger. The experimental setup in E791 consisted of vertexing and tracking devices, magnets to measure particle momenta, Čerenkov counters and calorimeters for particle identification and a specially designed data acquisition (DA) system to record the data at very high rate while the experiment was running. This chapter describes the E791 experimental setup, stressing parts that are most relevant to this analysis.

2.2 Beamline

E791 utilized a 500 GeV/c π^- beam incident on platinum and diamond targets. Protons from the main ring of the Tevatron at FNAL were extracted at 800 GeV/c and split to one of the three fixed-target experimental areas. The beam spill lasted for 23 s out of every 57 s. During each spill, about 2×10^{12} protons were incident on a 30 cm long beryllium target upstream of the E791 spectrometer. Pions resulting from this interaction

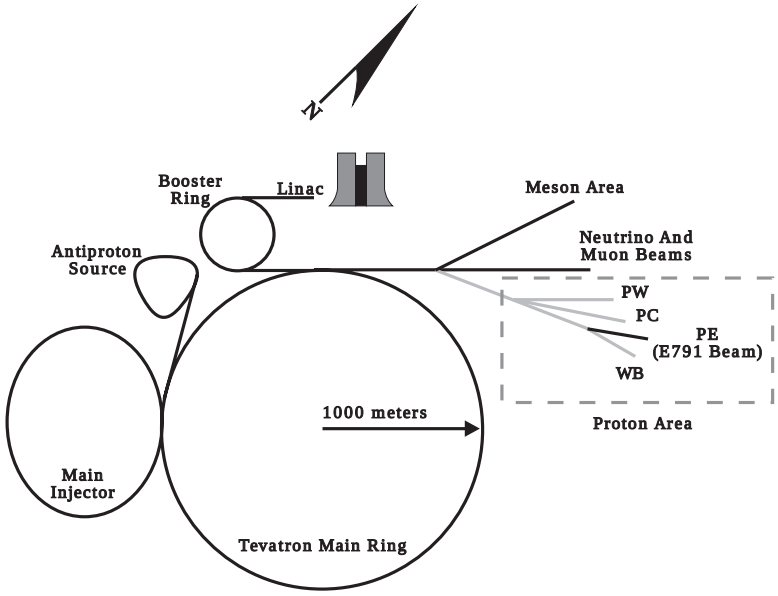

Figure 2.1: Layout of the Fermilab beam lines

were charge- and momentum-selected, then collimated into a beam of negatively charged pions with momentum (500 ± 20) GeV/c. The typical beam intensity was 2 million pions per second into the E791 hall. A schematic layout of the Fermilab beam lines is shown in Figure 2.1.

2.3 Target

The E791 target consisted of five thin foils, each separated by a distance of about 1.5 cm, as shown in Figure 2.2. The first (most upstream) target was made of platinum and was 0.5 mm thick. The remaining four targets were made of industrial-quality diamond, and were each 1.5 mm thick. The spacing of 1.5 cm between these thin targets ensured that the

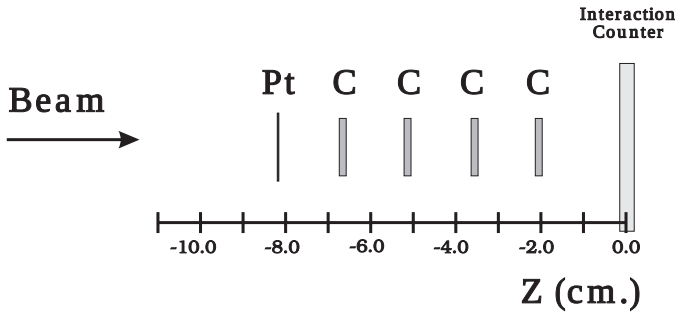

Figure 2.2: The schematic layout of the E791 target foils.

decay vertices of the weakly-decaying charmed particles were usually located outside the target, thus lowering background. The thinness of the target foils also made the detection of the primary vertex easier. With this target setup, the probability for a π from the beam to interact with the target was 2%.

2.4 E791 Spectrometer

The E791 spectrometer, as shown in Figure 2.3, consisted of detectors that performed position measurement (tracking and vertexing), momentum measurement and particle identification. Beam interaction and charm decay vertices were reconstructed using silicon microstrip detectors (SMD's), while downstream tracking was performed with drift chambers (DC's) and proportional wire chambers (PWC's). Two magnets were used to measure the momenta of charged particles. Particle identification was achieved using Čerenkov detectors, electronic and hadronic calorimeters and two muon walls. These detectors are described below.

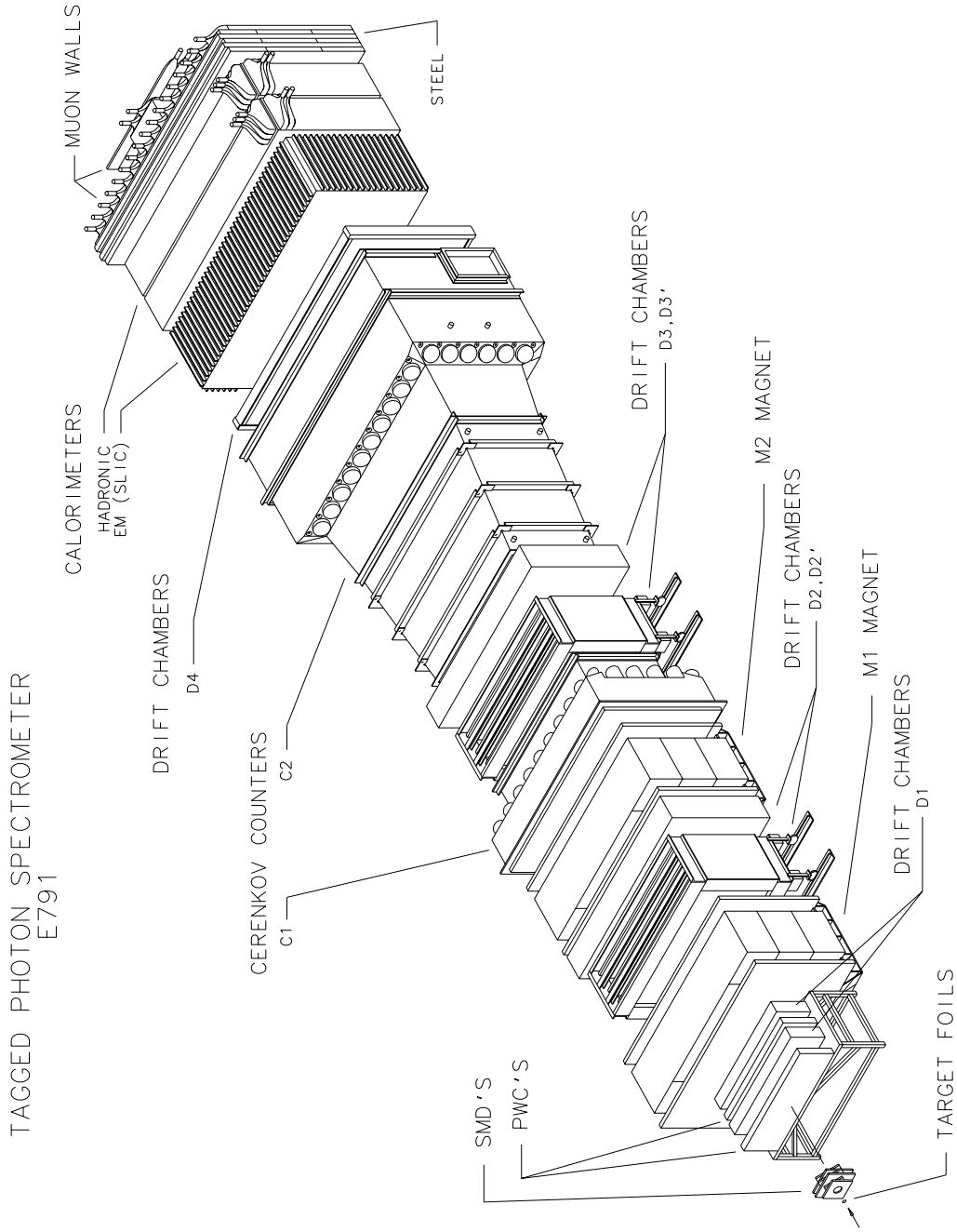

Figure 2.3: The E791 Spectrometer

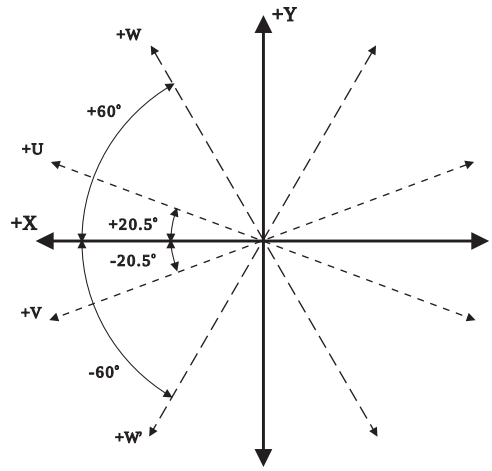

Figure 2.4: The E791 coordinate system showing x, y, u, v, w and w' axes. The z axis is going into the page.

2.5 E791 Coordinate System

It is useful to define the coordinate system used in E791 in order to describe the alignment of some of the detectors. It is a right-handed coordinate system, shown in Figure 2.4, with the z-axis very close to the beam direction and the y-axis pointing straight up from the ground. The origin is located just downstream of the targets.

In addition to x, y and z axes, E791 used u, v, w and w' directions to align the detectors. The u direction is at an angle of 20.5 degrees, and the w directions is at an angle of +60 degrees from the positive x axis towards the positive y axis in the xy plane. The v direction is at -20.5 degrees and the w' direction is at an angle of -60 degrees from the positive x direction towards negative y direction in the xy plane.

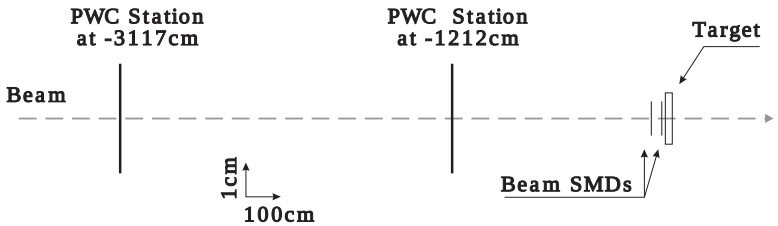

Figure 2.5: The schematic of upstream PWC-SMD system to track the beam.

2.6 Beam Tracking

Precise knowledge of the beam trajectory is helpful in locating the interaction point of the beam with the target, also known as the primary vertex. Beam trajectories were tracked by eight planes of proportional wire chambers and six planes of silicon microstrip detectors, as shown in Figure 2.5 and described below. The proportional wire chambers (PWC's) were located tens of meters upstream of the target in order to provide good angular resolution, while the SMD planes were located 30 to 80 centimeters upstream of the target system in order to precisely locate the interaction point. The beam profile near the target had a roughly gaussian distribution with a standard deviation (σ) of 0.2 cm in both x and y directions.

2.7 Vertex Reconstruction – Silicon Microstrip Detectors

Charm vertex reconstruction in E791 was performed with 17 silicon microstrip detector (SMD) planes, each 300 μm thick, located directly downstream of the targets. The resolution of the SMD's is determined by the center-to-center separation (the pitch) of the conducting aluminum strips deposited on the silicon. In some SMD planes, the pitch was smaller at the center, where track density is higher. The pitch and other characteristics of all the SMD planes are listed in Table 2.1. Spatial resolutions achieved by the SMD's

ranged from 7 to 15 μm in the direction perpendicular to the strips.

All SMD planes were oriented perpendicular to and centered on the z-axis, with the strips for each plane aligned perpendicular to either x, y, or v axes. The SMD's provided a geometric acceptance in a cone with a half-angle of 150 milliradians about the beam.

The distances of SMD planes from the target foils ranged from 3 to 50 cm. The precise measurement of particle trajectories by SMD's permitted secondary vertex positions to be measured with a resolution in the z direction of typically 470 μm (for $Kl\nu$ vertices), and about 340 μm for the primary vertex. This is adequate for measuring D^0 decays. For example, a 100 GeV/c D^0 decaying into $Ke\nu$ would have typically traveled a distance Δz of about 6672 μm before decaying. As the typical error on the the measured distance is $\sigma \sim \sqrt{470^2 + 340^2}$ μm $\sim$ 580 μm, thus $\Delta z/z \sim 11$.

2.8 Downstream Tracking – Drift Chambers and PWC's

E791 utilized 35 planes of drift chambers (DC's) and two planes of proportional wire chambers (PWC's) for tracking the charged particles downstream of the SMD's.

The 35 drift chamber planes measured track positions in x, u, and v directions. The ionizing medium in the drift chambers was a gas mixture consisting of 89% Argon, 10% CO_2 and 1% CF_4. These planes were divide into four modules: D1, D2, D3 and D4, labeled as such in Figure 2.3. Each of these modules consisted of one to four assemblies, with each assembly having three to four DC planes. The resolution of the DC planes ranged from 250 to 350 μm. The downstream PWC planes were only used for 'confirming' the tracks obtained from DC hits, i.e., a track formed from DC hits was projected to the PWC's to see if there was a corresponding hit. The characteristics of the PWC's and the DC's are described in Table 2.2 and Table 2.3 respectively.

SMD Characteristics						
Plane Number	Z Position (cm)	Size (cm^2)	Strip Pitch Inner; Outer (μm)	Num. Instr. Strips	View	Efficiency (%)
1	-80.250	1×1	25;50	384	Y	90
2	-79.919	1×1	25;50	384	X	90
3	-74.429	1×1	25;50	448	W	90
4	-33.163	1×1	25;50	448	W	90
5	-30.133	1×1	25;50	416	X	90
6	-29.483	1×1	25;50	416	Y	90
7	0.670	1.6×1.6	25;50	688	Y	89
8	1.000	1.6×1.6	50;50	688	X	89
9	1.931	2.6×2.6	50;50	512	X	94
10	3.015	2.6×2.6	50;50	512	Y	92
11	6.684	2.6×2.6	50;50	512	V	93
12	11.046	5×5	50;50	768	Y	93
13	11.342	5×5	50;50	768	X	93
14	14.956	5×5	50;50	768	V	95
15	19.915	5×5	50;50	1000	X	86
16	20.254	5×5	50;50	1000	Y	89
17	23.878	5×5	50;50	1000	V	91
18	27.558	10×10	50;200	864	V	93
19	31.848	10×10	50;200	864	X	90
20	34.548	10×10	50;200	864	Y	93
21	37.248	10×10	50;200	864	X	94
22	39.948	10×10	50;200	864	Y	95
23	45.508	10×10	50;200	864	V	93

Table 2.1: Characteristics of the E791 SMD system.

PWC Characteristics		
Parameter	Upstream Station	Downstream Station
Planes	8	2
Z Position (cm)	-3117 and -1212	118.5 and 161.1
Size (cm×cm)	6.4×3.2	53.0×28.8
Wire Spacing (cm)	0.01	0.02
Views	X, X' and Y, W	X, Y

Table 2.2: Characteristics of the E791 PWC systems.

DC Characteristics				
Parameter	D1	D2	D3	D4
Z Positions (cm)	142.5 to 183.7	381.4 to 500.8	928.1 to 1047.1	1738.0 to 1749.2
Planes	8	12	12	3
Assemblies	2	4	4	1
Views	X, X', U, V	U, X, V	U, X, V	U, X, V
U, V Cell Size (cm)	0.476	0.892	1.487	2.97
X, X' Cell Size (cm)	0.446	0.953	1.588	3.18
Size (cm×cm)	126×71	285×143	323×143	511×259
Resolution (μm)	400	300	300	450

Table 2.3: Characteristics of the E791 drift chambers.

2.9 Momentum and Charge Measurement – Magnets

E791 utilized two magnets to measure particle momenta and charges. To a good approximation, each magnet changes the transverse component (perpendicular to the z-axis) of the momentum of a track by a fixed amount, irrespective of the track momentum. This change in the transverse momentum is referred to as the p_T kick. p_T kicks for the two magnets were 212 MeV/c and 320 MeV/c respectively. Drift chamber planes just before and after the magnets measured bend angles, and hence momenta of individual tracks.

2.10 Particle Identification

Particle identification in E791 was achieved by using two threshold Čerenkov detectors, electromagnetic and hadronic calorimeters and two muon walls, as described below.

2.10.1 Čerenkov Detectors

The Čerenkov detectors were used in E791 mainly to identify the kaons, protons and pions. In order for a particle to emit Čerenkov radiation, it must have a momentum greater than a threshold value p_{th} which is given by:

$$p_{th} = \frac{mc}{\sqrt{n^2 - 1}} \tag{2.1}$$

where m is the particle mass and n is the index of refraction for the medium through which the particle is traveling. E791 utilized two segmented Čerenkov detectors, called C1 and C2 as shown in Figures 2.6 and 2.7. C1 and C2 had different threshold momenta for a given particle and provided differentiation between kaons, pions and protons in different momentum ranges [21]. For example, in the momentum range of 20 to 36 GeV/c, a pion would emit light in both C1 and C2, a kaon would emit light only in C1, and a proton would not emit light in either C1 or C2. Thus, depending on which Čerenkov detector(s) detect light from a given track, the particles can be identified if they are in appropriate

momentum ranges. Various parameters characterizing C1 and C2 are listed in Table 2.4, and the particle separation achieved in various momentum ranges is listed in Table 2.5.

Čerenkov Detector Characteristics		
Parameter	C1	C2
Medium	100% N_2	80% He, 20% N_2
$(n-1)$	290×10^{-6}	86×10^{-6}
p_{th} for π (GeV/c)	5.7	10.5
p_{th} for K (GeV/c)	20.2	38.5
p_{th} for p (GeV/c)	38.5	70.6
Number of Mirrors	28	32

Table 2.4: Some important characteristics of the two Čerenkov detectors C1 and C2. The threshold momentum for each Čerenkov detector indicates the point at which a given particle starts to emit Čerenkov radiation.

Čerenkov radiation in each detector was collected by spherical mirrors in a plane perpendicular to the z-axis. C1 and C2 had 28 and 32 mirrors respectively, arranged in a pattern as shown in Figure 2.8. The mirror sizes, listed in Table 2.6, are smaller near the beam axis to provide finer segmentation where the track density is high. Light incident on each mirror is reflected into Winston cones that funnel the incident light into a photomultiplier tube (PMT). The expected number of Čerenkov photons from a given particle is known as a function of momentum for each Čerenkov detector [21]. Based on this knowledge, a probability is assigned to each charged particle for being an electron, a muon, a pion, a kaon or a proton (although in E791 the Čerenkov detectors are only

Čerenkov Separation for π, K and p	
Momentum Range (GeV/c)	Separation Achieved
0 - 5.7	No Separation
5.7 - 10.5	π / K p
10.5 - 20.2	π / K p
20.2 - 37.1	π / K / p
38.5 - 70.6	π K / p
70.6 - 200.0	No Separation

Table 2.5: The Čerenkov separation for π, K, and p achieved in different momentum ranges.

useful to identify kaons, protons and pions).

Mirror No.	C1 (cm×cm)	C2 (cm×cm)
1	15.0×25.0	15.0×50.0
2	50.0×35.0	95.0×70.0
3	17.5×25.0	20.0×50.0
5	17.5×25.0	20.0×50.0
7	32.5×25.0	30.0×50.0
9	50.0×35.0	60.5×50.0
11	50.0×25.0	95.0×70.0
13	50.0×35.0	95.0×50.0
15		95.0×70.0

Table 2.6: Mirror sizes in one quarter of the Čerenkov mirror plane in C1 and C2. The dimensions are the width×the height.

2.10.2 Segmented Liquid Ionization Calorimeter (SLIC)

The segmented liquid ionization calorimeter (SLIC) [22] was used mainly to identify electrons and photons – particles that interact primarily through electromagnetic interaction, and thus was designed to maximize the energy deposition by these particles. The thickness of the SLIC is equivalent to 20 radiation lengths, so that most electrons and photons deposit all their energy in the SLIC, giving rise to well-contained showers. Hadrons and muons generally leave less energy, as the SLIC contains only 1.5 absorption lengths of material. A schematic view of the SLIC is shown in Figure 2.9.

The SLIC consists of 60 layers of lead and liquid scintillator, the thickness of each layer corresponding to one-third of a radiation length. Each liquid scintillation layer was optically separated into parallel strips by teflon-coated corrugated aluminum sheets which provided channels with total internal reflection surfaces. The scintillation light propagated along the axis of the strip, and was detected by a wavebar-phototube system at the end.

Each scintillating layer was 1.27 cm thick. The corrugations had a square-wave shape, with the width of each strip being 3.17 cm. The axes of the corrugation were at $\pm 20.5^\circ$ and 90° from the vertical, forming the u, v and y views respectively. The light generated in the scintillator layers propagated along the teflon channels via multiple total internal reflections. Much of the light emitted by the scintillating medium is in utraviolet range. Since PMT's are most sensitive in the visible range, this light was made to go through wavelength-shifter bars, which absorb the UV photons and re-emit in the visible range. PMT's glued to these waveshifter bars collected the light and converted it into electrical pulses.

The overall spatial resolution for locating the electron shower centroid was about 7 mm. The energy deposited by a charged particle or a photon is proportional to the light collected by the phototube, after correction for the attenuation in the scintillator and wavelength-shifter bars. Precise location of the shower position (centroid) resulted in tracks to be linked with showers, and the energy measurement (E) gave information on whether the track was an electron (or positron), by comparing E and the momentum p of the track. The important characteristics of the SLIC are listed in Table 2.7.

2.10.3 Hadronic Calorimeter

The hadronic calorimeter was located downstream of SLIC. A detailed description of the hadronic calorimeter can be found in reference 23.

The hadronic calorimeter detected the energy deposited by the hadrons. In order to maximize the energy loss by hadrons, the hadronic calorimeter was made of alternating

SLIC Characteristics	
Parameter	Value
Z position (cm)	1866 to 1962
Number of Channels	334
Usable Area (cm×cm)	490×240
Radiation Length	20
Absorption Length	1.5
Energy Resolution $\left(\frac{\Delta E}{E}\right)^2$	$(11.5\%)^2 + \left(\frac{17.4\%}{E}\right)^2$
Position Resolution (cm)	0.7

Table 2.7: Important Characteristics of the SLIC.

layers of steel (where the hadrons lose their energy) and plastic (scintillating material), providing a thickness of six interaction lengths. It was divided into front and back modules, each consisting of 18 plastic scintillator layers 3/8 inch thick. These scintillating layers were interleaved with 36 one inch-thick-steel plates. The hadronic calorimeter was segmented into two views, with separate scintillating plastic strips in the x and y directions forming the individual counters. The x counters spanned the full height of the detector, whereas the y counters were divided at the vertical midplane. Each module was read separately resulting in a total of 33 x counters and 38 y counters for 142 channels.

Since most of the electromagnetic showers were contained in the SLIC and the hadronic showers in the hadronic calorimeter, comparison of E_{had} and E_{SLIC} helped separate the electrons from hadrons, where E_{had} and E_{SLIC} are the energies deposited by a particle in the hadrometer and the SLIC respectively. For example, the ratio E_{had}/E_{SLIC} was found to be zero for 70% of the electrons and positrons in the 2-40 GeV/c momentum range. On the other hand, the ratio E_{had}/E_{SLIC} is zero for only 34% of charged pions (selected from K_s^0 decays) in the same momentum range. This fact was used to help achieve good e/π separation.

2.10.4 Muon Identification

As has been pointed out in previous sections, electrons, photons and hadrons are almost completely absorbed in the two calorimeters, while muons leave only a fraction of their energy in the calorimeters, mainly via ionization. Therefore, most of the particles that still survive after going through the two calorimeters and steel shielding are muons which can be easily detected with simple scintillating counters ("paddles"), attached to PMT's.

E791 used two walls of scintillation counters, called the X and Y muon walls, to identify muons. These walls were placed at the end of the spectrometer, behind steel shielding 106 cm thick which blocked hadrons. Only muons with momentum above 4 GeV/c passed through material equivalent of 239 cm of iron to reach the muon walls, producing light in the scintillation counters that was detected by the PMT's.

The first muon wall, called the X wall, consisted of 15 plastic scintillation counters housed in a light-tight box, and aligned vertically for measuring the x-position of the charged particles passing through it. Behind the X wall was a block of concrete partially overlapping with X and Y walls (Figures 2.10 and 2.11), with four paddles mounted behind the central X paddle. It was used in coincidence with the central X paddle in order to reduce noise in the central area that is directly in line with the beam. The second wall, called the Y wall, was situated 176 cm downstream from the X wall, and had 16 scintillating paddles of 14 cm width. The paddles in the Y wall were aligned horizontally to measure the y-position of the charged particle passing through them. The geometries of the X and the Y walls are shown in Figures 2.12 and 2.13 respectively.

As a charged particle went through the scintillating paddles, it emitted light which was collected by PMT's connected to each paddle via a light guide. Electrical pulses from the PMT's were sent into discriminators and also to time to digital converters (TDC's). The spatial resolution in the direction perpendicular to the paddles was determined by the paddle width. Some spatial resolution along the length of the paddles was obtained by TDC information, but it was not very good. Only the Y TDC information was used in this analysis, resulting in a spatial resolution of about 50 cm along the length of the Y paddles (see Appendix B). The efficiency of the X wall was measured to be $(69 \pm 3)\%$ and that of Y wall was found to be $(99 \pm 1)\%$ [24, 25]. The characteristics of the two muon walls are listed in Table 2.8.

2.11 Trigger and Data Acquisition System

E791 utilized very loose trigger requirements, recording events at a very high rate and with minimum bias. During the six month period ending in January 1992, about 50 Terrabytes of raw data were recorded on 24,000 8mm video tapes. An event was saved if the following criteria were satisfied:

Muon Wall Characteristics		
Parameter	X Wall	Y Wall
z-position (cm)	2243	2319 cm
Area (cm^2)	550×300	300×224
Number of paddles	15	16
Efficiency (%)	69 ± 3	(99 ± 1)

Table 2.8: Characteristics of the X and Y muon walls

- Only one beam particle was detected upstream of the targets. The number of beam particles was determined from the pulse height from a scintillating paddle called beam spot counter, placed in the beam path as shown in Figure 2.14.

- There was no signal in the beam halo counter, ensuring that the beam pion is not too far from the beam axis. The beam halo counter was a scintillating paddle with a 1 cm diameter hole at its center, as shown in Figure 2.14. The center of the hole was at the beam axis. If the beam pion strayed too far from the beam axis, it would cause a signal in the beam halo counter.

- At least four charged tracks were detected downstream of the target, as determined from the interaction counter shown in Figure 2.14. The interaction counter is a scintillating paddle. At the energies involved in the experiment, most of the charged particles are minimum ionizing, so that the amount of light generated in the scintillator is independent of their energy, and proportional to the number of charged

particles passing through. The number of tracks, therefore, was determined by comparing the pulse height from the interaction counter with a threshold that was set at a value corresponding to four minimum ionizing particles.

- $E_T > 4$ GeV/c, where E_T is the energy deposited in the SLIC (and hadrometer) transverse to the beam direction. E_T was calculated by taking the weighted sum of the raw signals from each calorimeter PMT, giving more weight to signals further from the beam axis.

- $E_T < 700$ GeV/c. This was required to reject events with multiple beam particles.

These loose triggering criteria resulted in a high trigger rate which was handled by a specially designed data acquisition (DA) system, described in detail in reference 26. Beam pions interacted with the target system every 25μs on average. About half of these interactions passed trigger requirements, resulting in about 50μs between triggered interactions.

A schematic of the DA system is shown in Figure 2.15. The beam spill lasted only 23 seconds, out of a 57 second beam spill cycle. Both the spill time and 34 seconds of interspill time time were utilized to write the recorded events to tape in a continuous manner. During the spill period, data segments from various detectors were digitized and sent to the DA system, at a rate of about 26 Mbytes/s. These data segments were temporarily stored into on of the eight FIFO (First In, First Out) memory buffers (80 MB each). These memory buffers then feed the data more slowly (utilizing also the dead time between the spills) to processors housed in six VME crates. The processors combined the data segments from various detectors into a single full event, approximately 3 Kbytes, and these events are then written to tape in parallel. A total of 42 Exabyte 8200 tape drives were used simultaneously to cope with the high rate of incoming data. The DA system was designed to deliver a maximum data rate to tape of about 9.6 Mbytes/s. However, during real data taking the throughput usually did not reach this limit.

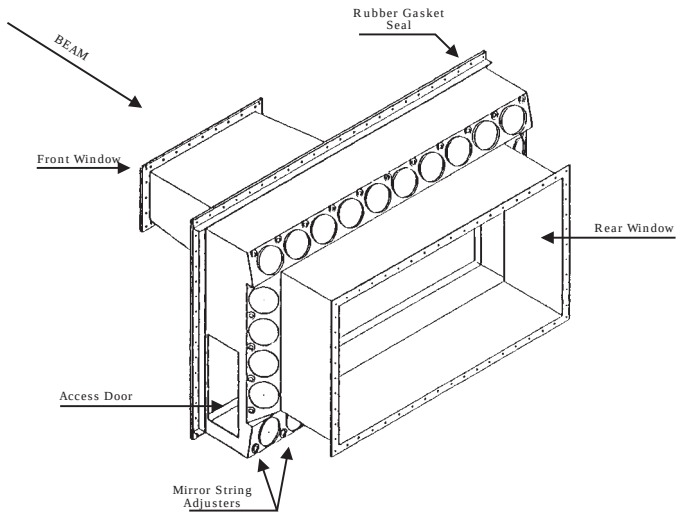

Figure 2.6: Schematic of the first Čerenkov detector, C1.

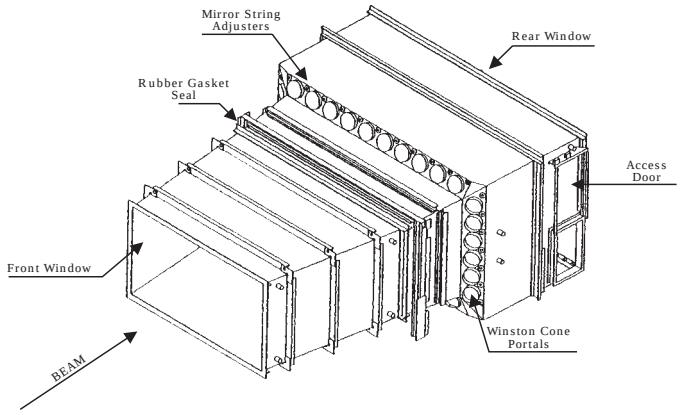

Figure 2.7: Schematic of the second Čerenkov detector, C2.

C1 MIRROR ARRAY

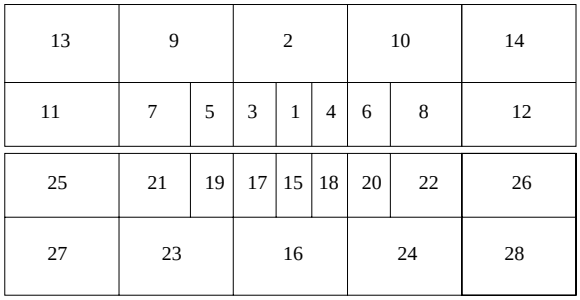

C2 MIRROR ARRAY

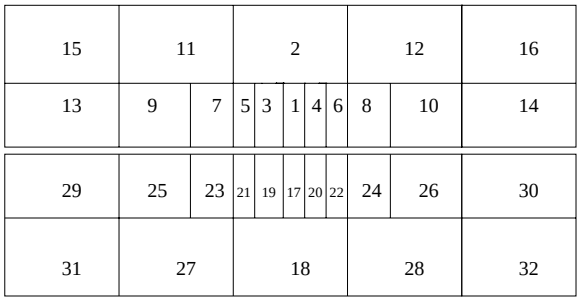

Figure 2.8: Schematic of the mirror segmentation in C1 and C2 Čerenkov detectors.

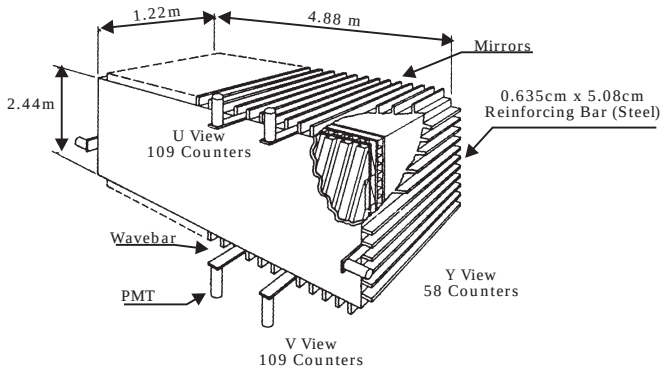

Figure 2.9: The schematic view of the SLIC.

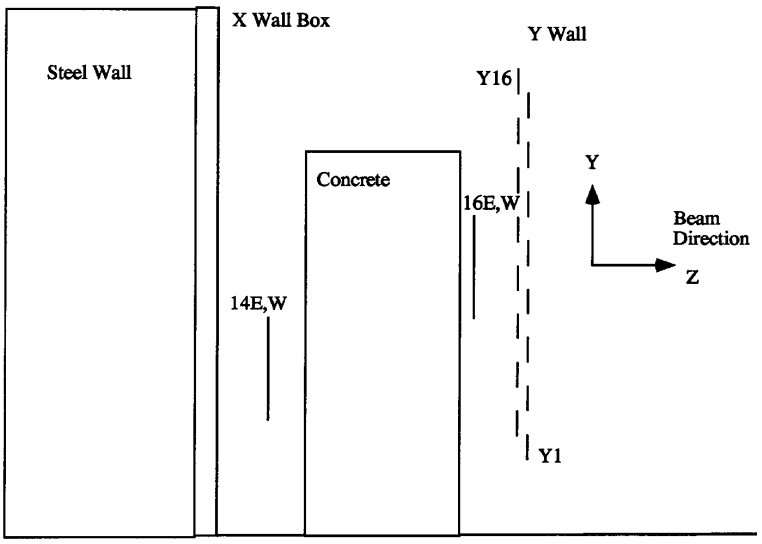

Figure 2.10: Side view of the muon system.

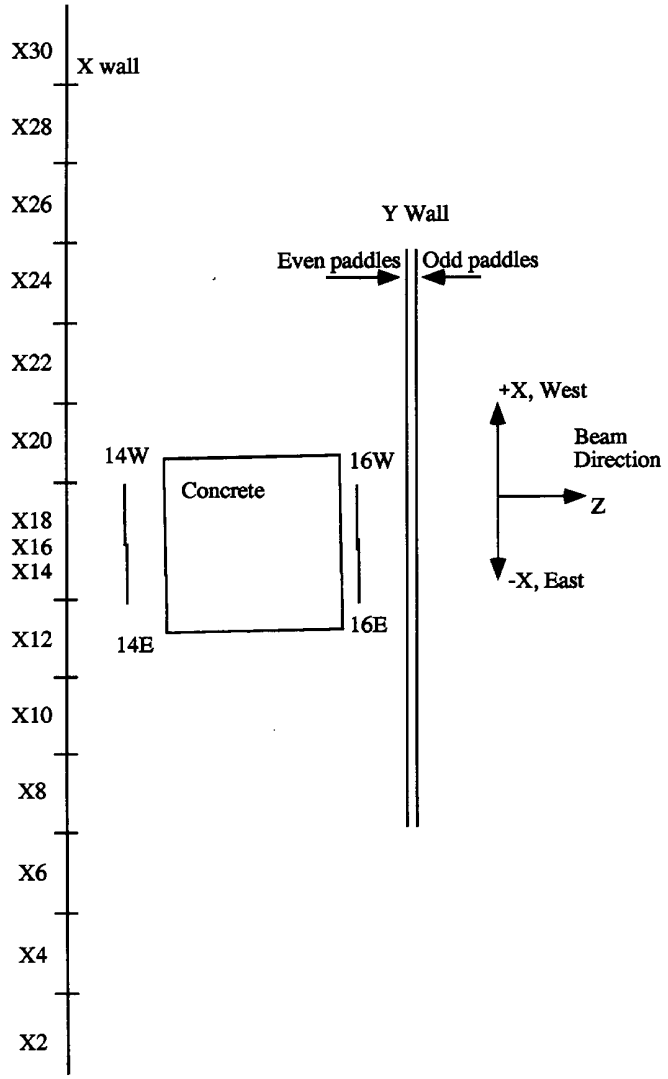

Figure 2.11: Top view of the muon system.

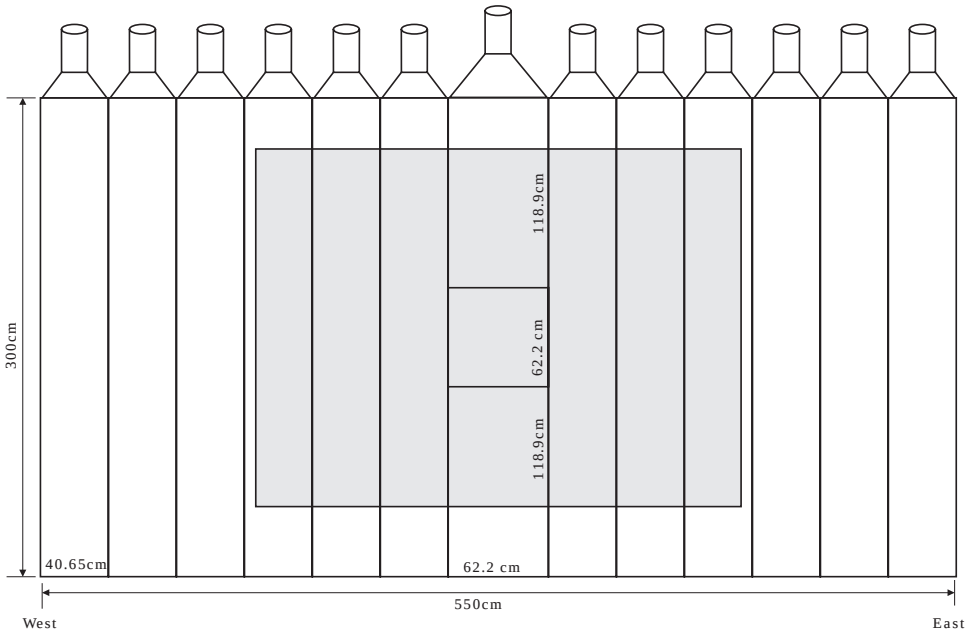

Figure 2.12: The geometry of the X muon wall. The shaded region shows the area of the X wall that overlaps with the Y wall.

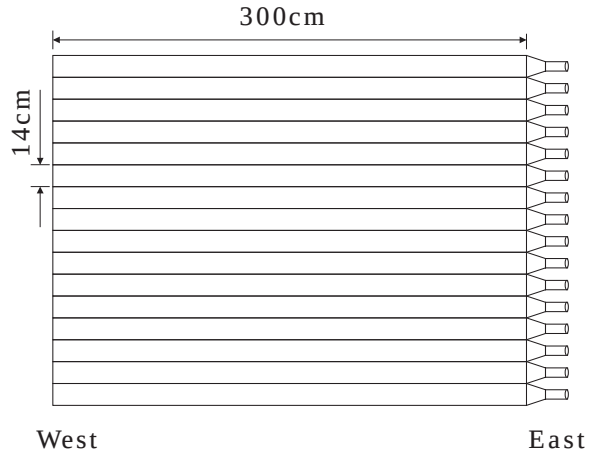

Figure 2.13: Geometry of the Y muon wall.

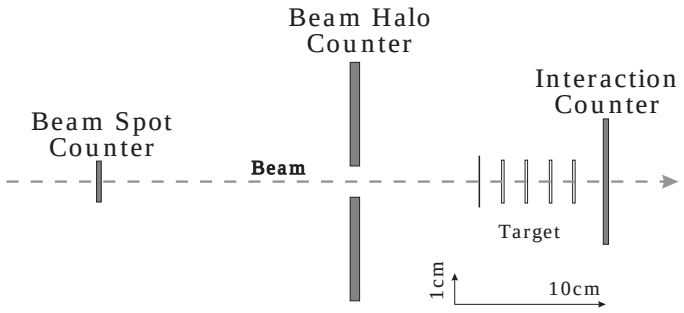

Figure 2.14: Schematic of scintillating paddles used in trigger decision.

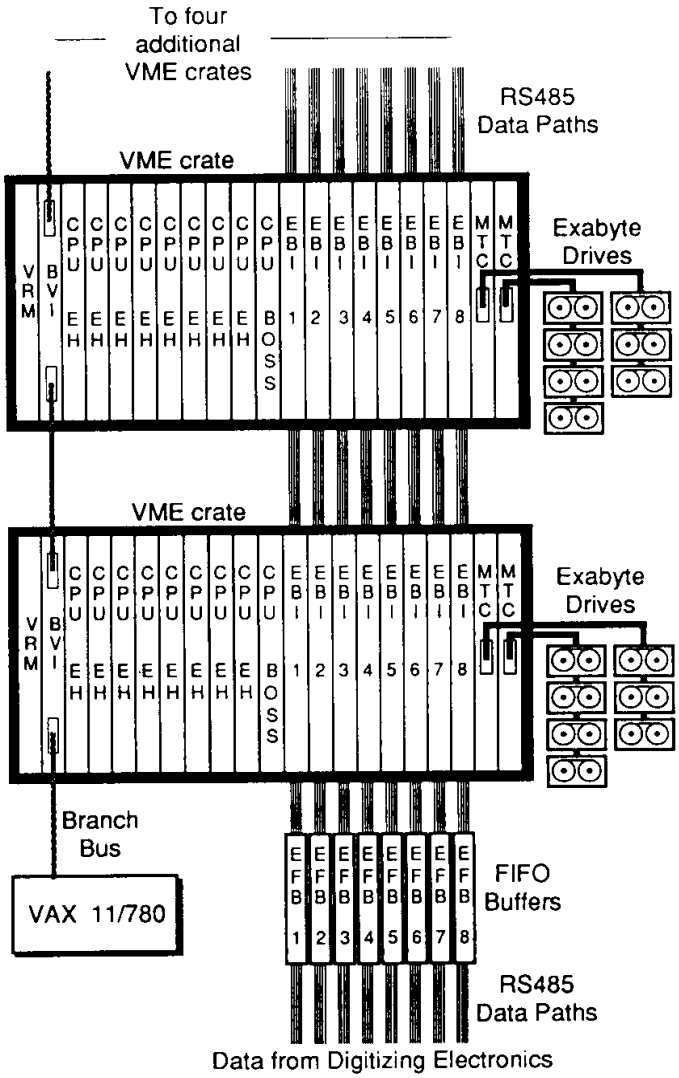

Figure 2.15: Schematic of the DA system used in E791.

Chapter 3

Data Reconstruction and Event Selection

3.1 Introduction

Due to the huge size (50 Terrabytes on 24,000 tapes) of data collected, a major challenge for E791 was to reduce this data to a manageable size while keeping the events with at least one charmed particle in them. Reduction was achieved in several steps. The first step in the process, known as event reconstruction and filtering, produced data summary tapes (DST's). These DST's then went through progressively more selective processes of stripping, substripping etc. These processes and the final selection criteria used for the semileptonic mixing analysis are described in this chapter. Figure 3.1 is a flow chart outlining the data-reduction process.

3.2 Event Reconstruction and Filtering

The data collected during the running of E791 consisted of compressed digital data segments from various parts of the spectrometer, e.g., SMD's, drift chambers, magnets,

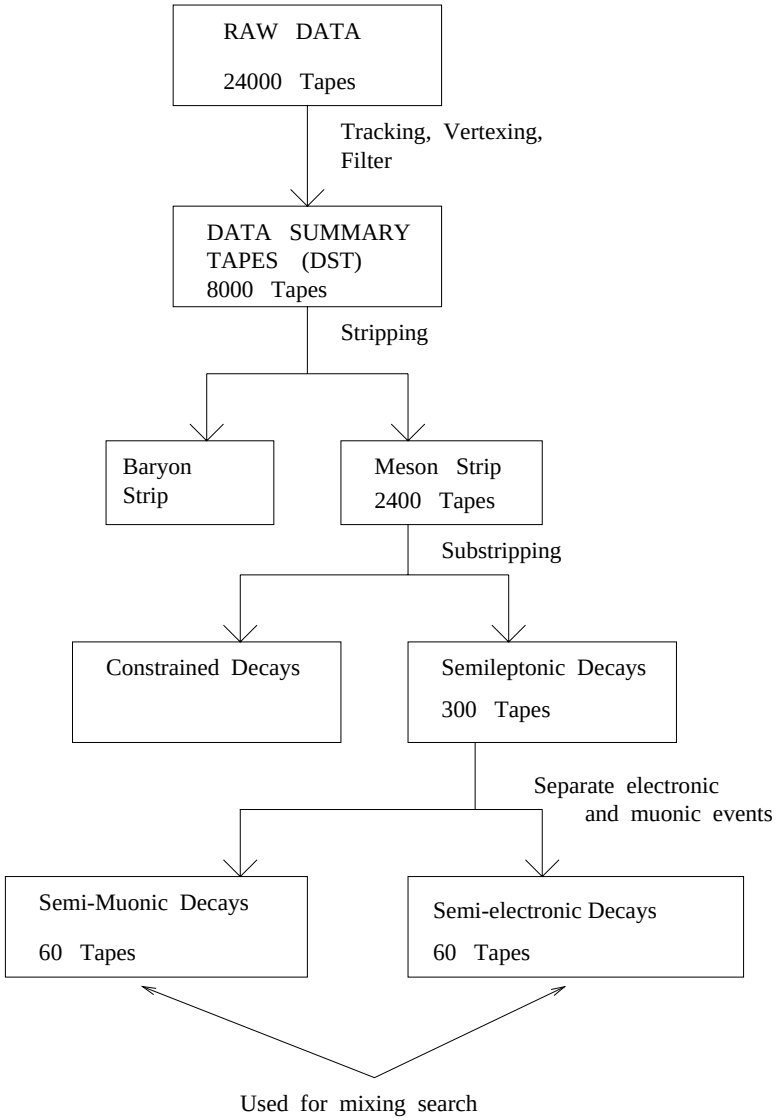

Figure 3.1: The flow chart outlining the process of data reduction.

calorimeters etc. Also, data from various detectors is in raw form, e.g., number of photons collected from each mirror in Čerenkov detectors; which strips in the SMD detectors were hit, etc. In the process of reconstruction, track and vertex reconstruction and particle identification were performed from the raw data, as described in section 3.2.1.

Event reconstruction was the most time-consuming process in data reduction, and took 2 years with 200 computers (9400 MIPS) at four different institutions (Kansas State University, Fermilab, University of Mississippi and Centro Brasileiro de Pesquisas) to complete.

3.2.1 Track and Vertex Reconstruction

Tracking data collected during the E791 run is in the form of hit locations in various tracking devices. Tracks were formed by fitting straight lines through hit positions. Once all charged tracks in an event were reconstructed, vertex reconstruction (or vertexing) was performed. The process of vertexing started with identifying the primary (interaction) vertex by intersecting the beam track with at least two downstream tracks. The primary vertex was constrained to be in or near a target foil, within measurement errors. After the primary vertex was found, secondary (decay) vertices were reconstructed from a set of all tracks with momentum greater than 2 GeV/c. Secondary vertex locations were found by combining two or more tracks which intersected within a specified volume (based on measurement errors) in space downstream of the primary vertex. The list of all such tracks, vertices and associated parameters (such as track slopes, vertex positions and their errors) were stored on data summary tapes (DST's).

3.2.2 Particle Identification

Particle identification was also performed during event reconstruction, which involved processing the raw data from the Čerenkov detector, electromagnetic and hadronic calorimeters and the two muon walls, and using it to assign a probability to a given charged track

of being a certain particle (π, K, p, μ, or e). Final particle identification criteria used in this analysis are described in sections 3.4.1, 3.4.2 and 3.4.3 below.

3.2.3 Filtering

During the reconstruction process, selection criteria were applied to reduce the bulk of the data while keeping most of the charm events. These selection criteria were general in nature, designed to save events with a broad range of physics analysis possibilities. This first stage of data reduction is known as 'filtering'. An event passed the filter if any of the following criteria was satisfied:

1. There must be at least two vertices (the interaction or primary vertex and a decay or a secondary vertex) in the event. In addition, a secondary decay vertex with two tracks must be separated from the primary vertex by at least $6\sigma_l$, and a secondary vertex with three or more tracks had to be separated from the primary vertex by at least $4\sigma_l$, where σ_l is error on the separation of the two vertices.
2. At least one K_s^0 is found in the event.
3. At least one Λ^0 is found in the event.
4. At least one ϕ is found in the event.
5. The event satisfied Pentaquark, B, or other physics tags.

The process of filtering kept most of the events containing charmed particles but rejected about 85% of the data, mainly due to the first requirement.

3.3 Further Data Reduction

After filtering, the total E791 data size was still 8000 tapes. In order to reduce this large data sample to a manageable size, additional selection criteria were applied in successive

stages known as stripping, substripping etc. A flow chart outlining these stages is shown in Figure 3.1. The details of the selection criteria applied at each stage shown in Figure 3.1 can be found in reference [27]. Only the final selection criteria used in this analysis will be described below, as they include all cuts applied at various data reduction steps.

3.4 Final Particle Identification Criteria

The decay of interest for this analysis is the D^*-D^0 decay chain in which the D^0 decays semileptonically. The topology of this decay chain is sketched in Figure 3.2. Both right- and wrong-sign events were kept, and identical selection criteria were applied to both the data samples.

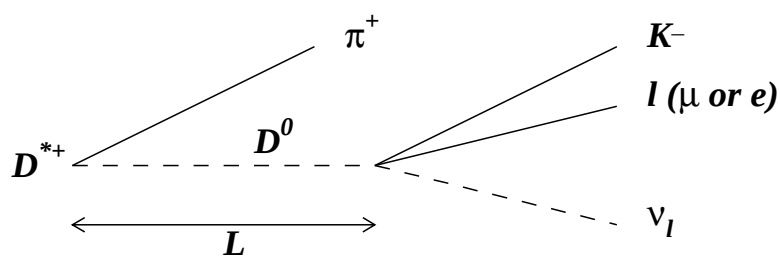

Figure 3.2: A schematic of the D^*-D^0 decay chain topology. The D^{*+} decays into a π^+ and a D^0. The D^0 subsequently decays into a semileptonic final state. This is an example of a Right Sign decay. The Wrong Sign decays, which would be a signature of mixing, have a similar topology, but the charge of the kaon from the D^0 decay is the same as the charge of the pion from the D^* decays.

The process of event selection started with searching for two-prong secondary vertices

containing a kaon and a lepton (e or μ); this required particle identification, as described below. Once such a secondary vertex was found, further selection criteria were applied in order to reduce background. Then a search was made for the pion from the D^* decay and the D^* Q-value was calculated, where $Q \equiv M(Kl\nu\pi) - M(D^0) - M(\pi)$. Only the candidates with $Q < 80$ MeV/c^2 were kept (for a true D^* decay, Q=5.8 MeV/c^2).

3.4.1 Kaon Identification

Kaons were identified in two threshold Čerenkov counters, as described in chapter 1. A detailed description of the Čerenkov particle identification process can be found in references [21] and [28]. For any given charged track, a probability called CPRB2 was calculated to be an electron, a muon, a pion, a kaon or a proton based on the information from the two Čerenkov detectors and also the calorimeters.

For the purpose of this analysis, a track was identified as a kaon if the corresponding CPRB2 for being a kaon was greater than 0.15. At this value, the average efficiency for detecting a kaon was approximately 0.62 and the average probability that a pion was misidentified as a kaon was 0.13.

3.4.2 Electron Identification

A detailed description of the electron identification in E791 can be found in references [29, 30]. A probability to be an electron was calculated for each charged track using the following measured quantities:

- $(E_{SLIC} - p)/\sigma_E$, where p is the measured momentum of the track and E_{SLIC} is the energy in the electromagnetic calorimeter associated with the track and σ_E is the error in the measured energy.
- The second moment of the SLIC energy distribution in the U or V views.

- The separation in X and Y of the shower centroid from the charged track positions in the SLIC.
- The energy in the hadronic calorimeter associated with the charged track.

Using the above quantities, a probability EMPROB for a track to be an electron was derived [30]. Values of EMPROB ranged from 0 to 100: The larger the value of EMPROB for a given track, the more likely it is to be an electron. For the purpose of this analysis, a track was identified as an electron if it had an EMPROB of at least 80. At this value of EMPROB, the average probability that a $\pi(K)$ is misidentified as an electron is 1.6%(0.8%). These misidentification probabilities were obtained from the large D^+ sample available in E791. In the decay $D^+ \rightarrow K^-\pi^+\pi^+$, the kaon and the pions can be identified by their charge alone (the kaon is the track with the charge opposite to that of the vertex, and the other two tracks are pions). The misidentification rates were measured by applying different EMPROB cuts on these samples of known kaons and pions.

Electron identification efficiencies were measured using photoconversion electrons. The electron identification efficiency depends on the value of the EMPROB and on track momentum. For an EMPROB value of 80, the electron identification efficiency varied from 0.72 in the 0 to 6 GeV/c momentum range to 0.61 for the tracks with momentum greater than 20 GeV/c [29].

3.4.3 Muon Identification

Muons were identified in two walls of scintillating counters behind shielding equivalent to 2.5 meters of steel, as described in chapter 2.

For this analysis, only tracks with momentum greater than 10 GeV/c which had hits in the drift chamber D3, and which pointed at the muon walls, were considered as muon candidates. The cut on track momentum was applied in order to reduce decays in flight. The X and Y coordinates of such tracks at the muon walls were found by projection.

Since muon candidates went through approximately 13 interaction lengths of material prior to hitting the muon walls, they suffered considerable multiple scattering, causing an uncertainty in their projected positions. If the projected position of the track fell within a muon paddle registering a hit, the track was considered as a muon candidate. If the projected position was away from a hit paddle, then the track was considered to be a muon candidate if the distance of the projected position of the track from the edge of the nearest hit paddle was within 1.64σ, where σ was the standard deviation of the multiple scattering distribution corresponding to the momentum of the track. It was empirically given by:

$$\sigma_x = \frac{55.62}{p - 1.29} \text{ cm} \tag{3.1}$$

$$\sigma_y = \frac{98.55}{p - 1.87} \text{ cm}, \tag{3.2}$$

where p is the track momentum, and σ_x and σ_y are the widths of multiple scattering distributions at the X and Y walls. These equations were obtained from Monte Carlo simulations of scattering through the SLIC, Hadronic Calorimeter and steel [24].

A quantity called MUCAT, which ranged from 0 to 10, was calculated for every muon candidate. The higher the value, more likely that a given track really was a muon. The TDC information was also used in the Y wall. Appendix B describes how MUCAT was calculated and how TDC information was used. For the final analysis, a track was considered to be a muon if *at least one* of the following criteria was satisfied:

a. MUCAT ≥ 7, that is, there is a coincidence between X and Y walls.

b. MUCAT ≤ 6, AND the track is outside Y-wall acceptance. These tracks hit the X wall on its periphery, away from the central congested region. Since the density of tracks on the periphery is low, there is less confusion while matching hits with a track and a fairly clean sample of muons is obtained this way.

c. MUCAT ≤ 6, AND the track is inside Y-wall acceptance, and the projected X-position of the track on the Y-wall is within 50 cm of the position predicted by TDC information. MUCAT ≤ 6 corresponds to the muon candidates that had a hit only in the Y wall, and there was no corresponding hit in the X wall. However, Y-wall TDC information was used to predict the approximate X position of the hit as described in Appendix B.

3.5 Final Selection Criteria

The final event selection criteria for this analysis were guided by judging the effect of a cut on $Kl\nu$ signals from Monte Carlo simulations and background from real data. Figure 3.3 shows Monte Carlo Q-value distributions for $Ke\nu$ and $K\mu\nu$ modes (the momentum of D^0 has to be estimated in order to calculate Q-value, see chapter 4 for a description of how it was done). The MC events with $Q < 20$ MeV/c^2 were considered as signal, and real data events with $Q > 25$ MeV/c^2 (where no signal is expected) were used to model background for the cut optimization process.

Both the $Ke\nu$ and $K\mu\nu$ modes had several common features, so that the description of the selection criteria is separated into two parts – one that is common to both decay modes, and the other that is not.

3.5.1 The Selection Criteria Common to $Ke\nu$ and $K\mu\nu$ Modes

1. The secondary vertex must be separated from the primary vertex by $8\sigma_L$, where L is the separation between the primary and the secondary vertices.

2. One of the tracks in the two-prong secondary vertex must be identified as an electron (section 3.4.2) or as a muon (section 3.4.3).

3. The other track in the secondary vertex must be identified as a kaon in the Čerenkov detectors, as described in section 3.4.1.

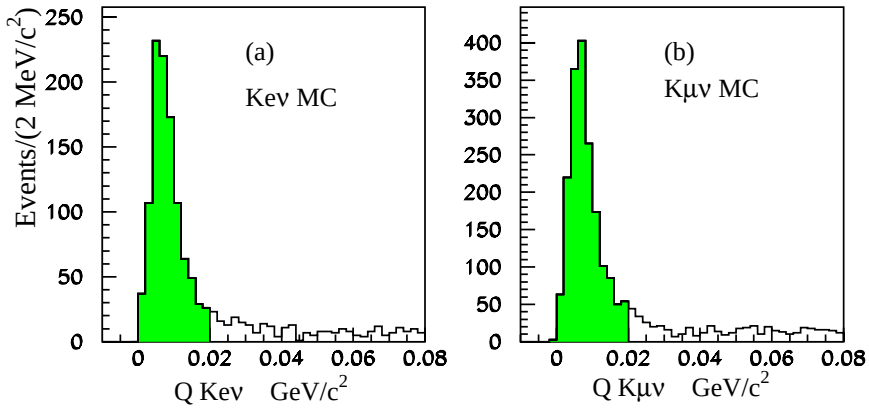

Figure 3.3: Q-value distributions for Monte Carlo $Ke\nu$ and $K\mu\nu$ signals, where $Q \equiv M(Kl\nu\pi) - M(D^0) - M(\pi)$. The events in the shaded area ($Q < 20$ MeV/c^2) were used to model the signal while choosing the final selection criteria. The background was modeled from real data events with $Q > 25$ MeV/c^2, where no signal is expected.

4. Each track in the secondary vertex, when projected back, must miss the primary vertex by at least 70 μm. This ensures that the secondary vertex did not include one or more tracks coming from the primary vertex.

5. The secondary vertex must be at least 3σ outside the edge of the nearest solid material. This cut was applied in order to minimize secondary interactions.

6. $1.6 < M_{min} < 2.1$ GeV/c^2, where $M_{min} = P_T + \sqrt{P_T^2 + M_{Kl}^2}$. P_T is the total transverse momentum of the charged decay products w.r.t. the direction of flight of the D^0, and M_{Kl} is the invariant mass of the charged decay products (Kl). Figure 3.4 shows the M_{min} distributions for the Monte Carlo (MC) $Ke\nu$ signal (solid line) and real-data background (dashed line) events. M_{min} distribution for true $Kl\nu$ decays has a cusp at D^0 mass, and falls rapidly at lower values. The non-charm background, on the other hand, peaks at low values of M_{min}. This cut

reduces the non-charm background while keeping majority of the $Kl\nu$ events.

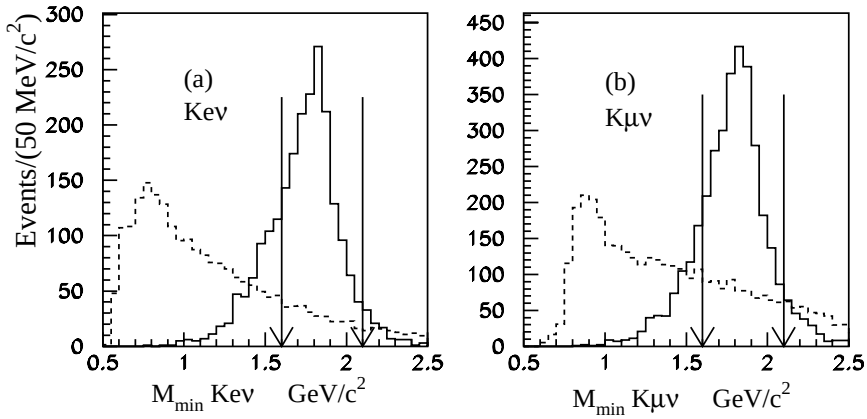

Figure 3.4: M_{min} distributions for MC signal (solid line) and data background (dashed line) events. The arrows indicate the cut $1.6 < M_{min} < 2.1$ GeV/c^2.

7. $1.15 < M_{Kl} < 1.8$ GeV/c^2, where M_{Kl} is the invariant mass of the charged decay products of the D^0. The motivation for this cut is the same as that for M_{min} above. Figure 3.5 shows M_{Kl} distributions for Monte Carlo $Kl\nu$ signal (solid line) and data background (dashed line) events. For true $Kl\nu$ decays, the M_{Kl} distribution cuts off at 1.8 GeV/c^2, and peaks at approximately 1.4 GeV/c^2. The lower cut on M_{Kl} again reduces non-charm background. The upper cut on M_{Kl} eliminates feedthrough into the semileptonic sample from the hadronic decay mode $D^0 \rightarrow K^-\pi^+$ in which the pion is misidentified as a lepton. This is evident from Figure 3.6, in which invariant mass of all Kl candidates is plotted under $K\pi$ hypothesis for RS and WS in each mode. There are no events beyond approximately 1.8 GeV/c^2, due to the upper cut on M_{Kl}. There would be a peak at D^0 mass (1.8645 GeV/c^2) if this feedthrough were present.

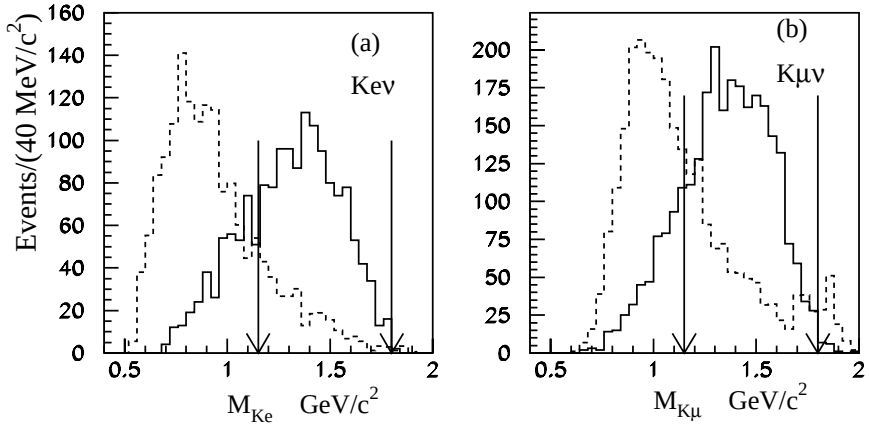

Figure 3.5: M_{Kl} distributions for MC signal (solid line) and data background (dashed line) events. The arrows show where the cuts were placed, i.e., $1.15 < M_{Kl} < 1.8$ GeV/c^2.

8. The total transverse momentum P_T of the visible decay products (Kl) with respect to the direction of flight of the D^0 must be greater than 1.5 GeV/c. Maximum kinematically allowed P_T in such decays is approximately 0.9 GeV/c. This cut was intended to remove vertices that had very high P_T due to large measurement errors on the vertex positions.

9. The transverse momentum of the kaon with respect to the direction of flight of the D^0 must be greater than 0.4 GeV/c and that of the lepton must be greater than 0.2 GeV/c. Figures 3.7 and 3.8 show the distributions of these quantities for Monte Carlo signal (solid line) and data background (dashed line) events. These cuts again reduce non-charm background, since charm decays tend to have higher transverse momenta.

10. $|M_{\pi K} - M_{D^0}| > 30$ MeV/c^2, where $M_{\pi K}$ is the invariant mass of the Kl candidate

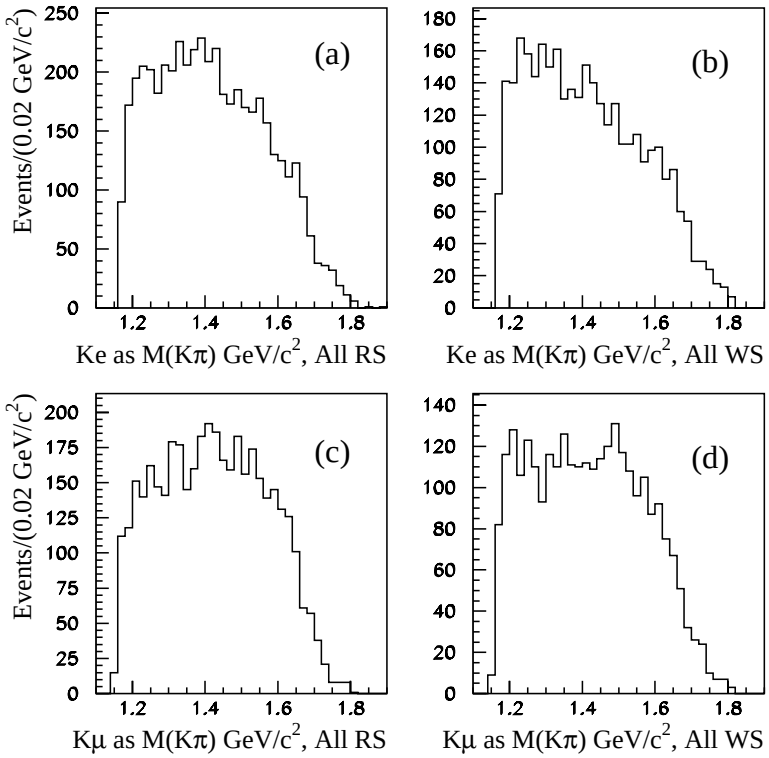

Figure 3.6: Mass spectrum of the $K - l$ vertices when the lepton is assigned the π mass. There are (almost) no events beyond 1.8 GeV. There would be a peak at D^0 mass (1.8645 GeV) if Kπ events were feeding into the semileptonic data sample.

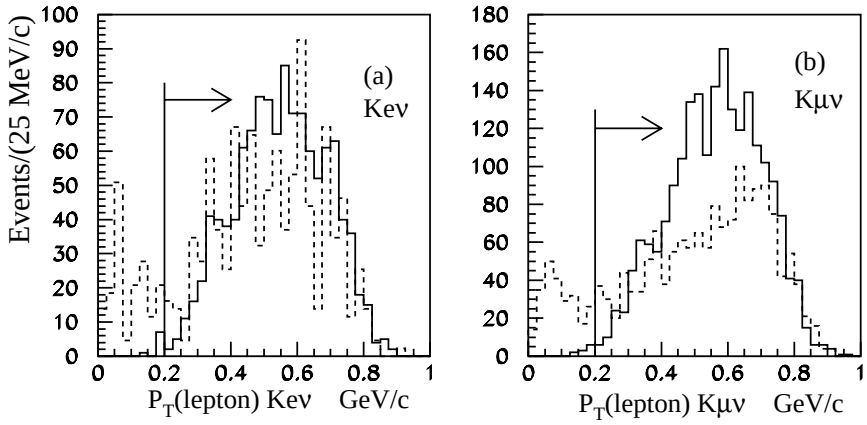

Figure 3.7: The distributions of P_T^l, the transverse momentum of the charged lepton w.r.t. the direction of flight of D^0, for MC signal (solid line) and data background (dashed line) events. The arrow shows the cut $P_T^l > 0.2$ GeV/c

.

when the lepton is assigned the kaon mass and the kaon is assigned the pion mass. This cut is designed to get rid of doubly misidentified $D^0 \rightarrow K^-\pi^+$ decays in which the kaon is misidentified as a lepton and the pion is misidentified as a kaon. Such misidentification, although expected to be small, would result in a peak in the wrong-sign sample at approximately correct D^* mass and must be removed while searching for a rare process such as mixing.

11. The estimated proper decay time of the D^0 must be less than 3 ps (calculation of lifetime involves estimating the neutrino momentum, see Chapter 4 for a description of how it was done). This corresponds to more than seven times the mean life time of the D^0, and would keep nearly all of the signal, including longer-lived mixed decays.

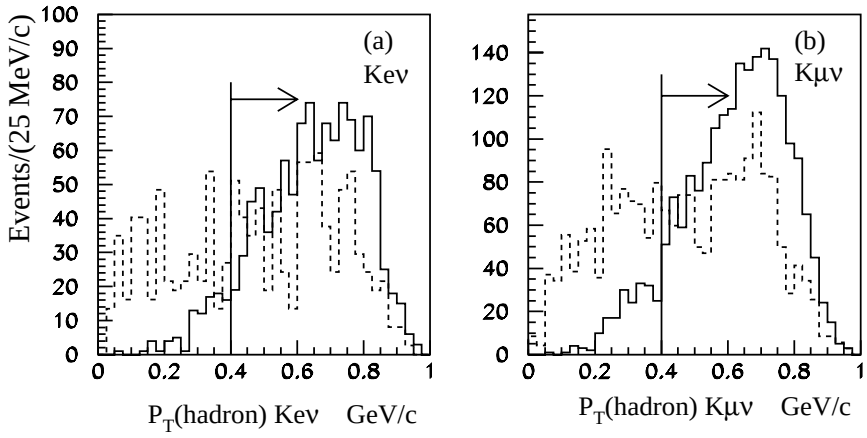

Figure 3.8: The distributions of P_T^h, the transverse momentum of the hadron w.r.t. the direction of flight of D^0, for MC signal (solid line) and data background (dashed line) events. The arrow shows the cut $P_T^h > 0.4$ GeV/c.

12. The fit χ^2 per degree of freedom of all the tracks in the $D^* - D^0$ decay chain must be less than 6.5.

13. The momentum of the pion from D^* decay must be greater than 2 GeV/c. This cut was aimed at reducing combinatoric background which arises when a low-momentum random pion from the primary vertex is combined with a D^0 candidate.

14. The pion from D^* must be consistent with coming from the primary vertex. Since D^{*+} decays strongly, it can not travel a measurable distance between production and decay.

3.5.2 Cuts Used in $Ke\nu$ Analysis Only

1. $M^{ee}_{min} > 40$ MeV/c^2, where M^{ee}_{min} is the minimum invariant mass when the electron candidate from the D^0 vertex is combined with all other oppositely charged tracks in the event. This cut is aimed at reducing contamination from photoconversion electrons. Figure 3.9 shows M^{ee}_{min} distributions for MC signal (solid line) and data background (dashed line) events. There is a big peak in the background distribution at low values of M^{ee}_{min}, which is rejected by the cut with little loss of the signal.

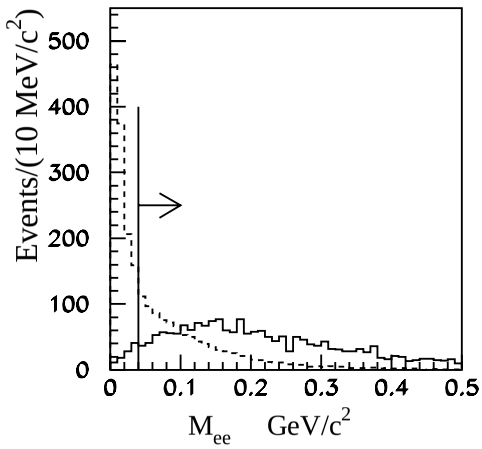

Figure 3.9: M^{ee}_{min} distributions for MC $Ke\nu$ signal (solid line) and data background (dashed line). The arrow indicates the cut $M^{ee}_{min} > 40$ MeV/c^2.

3.5.3 Cuts Used in $K\mu\nu$ Analysis Only

1. If a muon candidate is also found to be consistent with a kaon based on the Čerenkov information, reject the vertex.

2. $|M_{KK} - M_{D^0}| > 30$ MeV/c^2, where M_{KK} is the invariant mass of the Kl vertex when both the hadron and the lepton are assigned the kaon mass. This cut is aimed at eliminating feedthrough from the decay $D^0 \to K^+K^-$, when one of the kaons is misidentified as a muon (or correctly identified as muon after decay in flight). Such misidentified decays, if not eliminated, would feed into both the right- and wrong-sign samples.

Events that passed all selection criteria described in the previous sections were used in the fit to search for a mixing signal, as described in the next chapter.

Chapter 4

The Analysis and Fitting Technique

4.1 Introduction

This chapter describes in detail the analysis and fitting techniques used to search for a mixing signal. Events that passed the final selection criteria, as described in chapter 3, were used for the mixing search. For each event, the Q-value ($Q \equiv M(Kl\nu\pi) - M(D^0) - M(\pi)$) and proper decay-time t were calculated. Final results were obtained by applying an unbinned maximum likelihood fit to the final data sample.

4.2 Calculation of Q and t

In order to calculate the Q-value and proper decay time t of the D^0 for a given event, the momentum of the D^0 has to be known. However, there is an undetected neutrino in semileptonic decays so that the D^0 momentum cannot be measured and has to be estimated. Fortunately, it is possible to solve for the neutrino momentum up to a 2-fold ambiguity using vertexing information and the measured momenta of D^0 charged decay

products. It is algebraically simpler to work in a frame of reference (denoted by a *) in which the Z-axis is along the direction of flight of D^0, and

$$P_Z^{Kl} \equiv P_Z^K + P_Z^l = 0. \tag{4.1}$$

It can be shown that the energy of the neutrino in this reference frame is given by:

$$E_\nu^* = P_\nu^* = \frac{M_{D^0}^2 - M_{Kl}^2 - 2P_T^2}{2E_{Kl}^*} \tag{4.2}$$

where M_{Kl} is the invariant mass, and P_T is the total transverse momentum of the visible decay products with respect to (w.r.t.) the direction of flight of the D^0 (i.e., the Z-axis). It has been assumed that the neutrino is massless. E_{Kl}^* is the total energy of the visible decay products in the * frame:

$$E_{Kl}^* = E_K^* + E_l^* \tag{4.3}$$

The value of E_{Kl}^* can be obtained by boosting the known lab quantities back to this frame:

$$E_{Kl}^* = \gamma[E_{Kl}^{Lab} - \beta(P_{Kl}^Z)^{Lab}] \tag{4.4}$$

where

$$\beta = \frac{(P_{Kl}^Z)^{Lab}}{E_{Kl}^{Lab}} \quad \text{and} \quad \gamma = \frac{1}{\sqrt{1-\beta^2}} \tag{4.5}$$

Having obtained the total neutrino momentum in the * frame, one can immediately get the longitudinal momentum of the neutrino:

$$(P_\nu^Z)^* = \pm\sqrt{(P_\nu^*)^2 - P_T^2} \tag{4.6}$$

This momentum can then be boosted to the lab frame:

$$(P_\nu^Z)^{Lab} = \gamma[(P_\nu^Z)^* + \beta E_\nu^*] \tag{4.7}$$

$(P_\nu^Z)^{Lab}$ can be combined with the measured lab momenta of the hadron and lepton to obtain D^0 momentum. However, there are two solutions to equation 4.6, and there is no unique way to tell which one is correct. Since Monte-Carlo studies indicate that the positive solution was correct for E791 about 65% of the time, the positive solution was used for all events, so as not to bias the signal. The root mean square (RMS) deviation from the true value of the momentum estimated in this way is 15%, based on Monte-Carlo studies.

Using this momentum estimate, the Q-value and proper decay time t for each event were calculated. The final Q-value distributions for the $Ke\nu$ and $K\mu\nu$ modes are shown in Figure 4.1. Large clean signals are seen in the right-sign plots (Figures 4.1(a) and 4.1(b)).

4.3 Maximum Likelihood Fit

An unbinned maximum likelihood fit was performed on the final data sample to extract the mixing rate. This process requires shapes of Q and t distributions for the signal and background. Fits to the *right-sign* and *wrong-sign* data were done simultaneously. Only the events with Q $<$ 60 MeV/c^2 and proper decay time $t < 3.0$ ps were used.

4.3.1 Likelihood Function

The fits to $Ke\nu$ and $K\mu\nu$ data samples were done separately, but the likelihood functions were identical for both samples. The final log-likelihood $\mathcal{L}$ was a sum of two functions, one for the right-sign and the other for the wrong-sign events:

$$\mathcal{L} = \mathcal{L}_{RS} + \mathcal{L}_{WS} \tag{4.8}$$

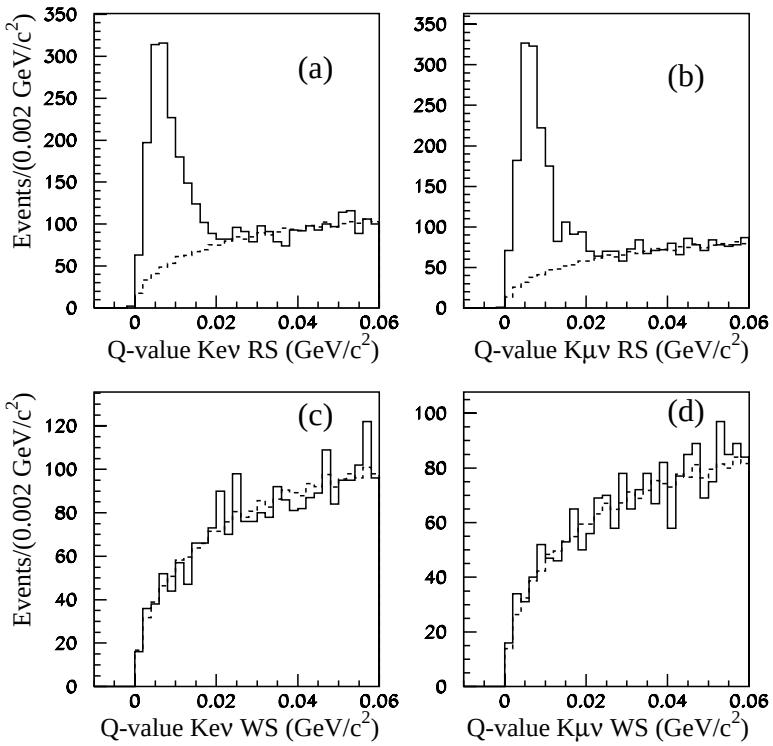

Figure 4.1: Q-value distributions for $Ke\nu$ and $K\mu\nu$ modes after the final cuts. The solid histograms are the distributions from data, and the dashed histograms are from event-mixing, normalized to the number of events in the region Q $>$ 20 MeV/c^2 for each plot. The top two plots (a and b) are for right-sign, and the bottom two (c and d) for wrong-sign events. There is no visible evidence for a signal in the wrong-sign plots.

$\mathcal{L}_{RS}$ is given by the equation:

$$\mathcal{L}_{RS} = -\sum_{i=1}^{N^{RS}} \ln(L_i^{RS}) + \frac{(N_{obs}^{RS} - N_{pred}^{RS})^2}{2N_{pred}^{RS}} + 0.5\ln(N_{pred}^{RS}) \tag{4.9}$$

N_{obs}^{RS} is the total *observed* number of right-sign events in the fit, and N_{pred}^{RS} is the total number of right-sign events *predicted* by the fit. The last two terms on the right-hand side of equation 4.9 put a Gaussian constraint on the total number of right-sign events predicted by the fit, since this number is known within statistical errors and is equal to the total numbers of RS events being fit. L_i^{RS} is the likelihood for the ith RS events, described by equation 4.11 below.

The log-likelihood for the wrong-sign events is given by a similar equation:

$$\mathcal{L}_{WS} = -\sum_{i=1}^{N} \ln(L_i^{WS}) + \frac{(N_{obs}^{WS} - N_{pred}^{WS})^2}{2N_{pred}^{WS}} + 0.5\ln(N_{pred}^{WS}) \tag{4.10}$$

where N_{obs}^{WS} is the total *observed* number of wrong-sign events, and N_{pred}^{WS} is the total number of wrong-sign events predicted by the fit. L_i^{WS} is the likelihood function for the ith wrong-sign event, described by equation 4.12 below.

The likelihood function for the ith event of each kind (RS and WS) is defined as:

$$L_i^{RS} = \frac{N_s^{RS} f_s(Q, Q_0, \sigma_L(t), \sigma_R(t)) F_s^{RS}(t) + N_b^{RS} f_b(Q) F_b(t)}{N_s^{RS} + N_b^{RS}} \tag{4.11}$$

$$L_i^{WS} = \frac{N_{mix} f_s(Q, Q_0, \sigma_L(t), \sigma_R(t)) F_s^{MIX}(t) + N_b^{WS} f_b(Q) F_b(t)}{N_{mix} + N_b^{WS}} \tag{4.12}$$

In the above equations, N_s^{RS} = number of right-sign signal events and N_b^{RS} = number of right-sign background events, N_{mix} = number of mixed events in the WS data sample, N_b^{WS} = number of WS background events.

Function $f_s(Q, Q_0, \sigma_L(t), \sigma_R(t))$ describes the shape of the signal in Q-value, and $f_b(Q)$ describes the shape of the background in Q-value, as discussed below. Note that these

functions do not have a RS or WS superscript associated with them, since they are identical for both RS and WS decays. The RS and WS decays are kinematically identical, and therefore the shape of both the RS and WS signals are expected to be identical in Q-value. The background in both RS and WS decays consists of mainly real D^0's combined with random pions and also some purely random combinatoric background (arising when random tracks combine to form a D^0 vertex), which are again expected to be the same for both RS and WS samples.

Function $F_b(t)$ describes the shape of the decay-time distribution for background events in both RS and WS samples. $F_s^{RS}(t)$ describes the shape of the RS signal decay-time distribution, and $F_s^{MIX}(t)$ describes the shape of the decay-time distribution for the mixed decays. These functions are described below.

The function $f_s(Q, Q_0, \sigma_L(t), \sigma_R(t))$ used to describe the shape of the signal Q-value distribution (for both RS and WS) is parametrized as:

$$f_s(Q, Q_0, \sigma_L(t), \sigma_R(t)) = \begin{cases} Ae^{\frac{-(Q-Q_0)^2}{2(\sigma_L(t))^2}} & \text{if } Q \leq Q_0 \\ Ae^{\frac{-(Q-Q_0)^2}{2(\sigma_R(t))^2}} & \text{if } Q > Q_0 \end{cases} \tag{4.13}$$

A is a normalization factor such that the integral of f_s over the whole fit range is unity.

$\sigma_L(t)$ and $\sigma_R(t)$ are decay-time dependent widths, parametrized as:

$$\sigma_L(t) = \sqrt{(\sigma_L^0)^2 + (C_L/t)^2} \tag{4.14}$$

$$\sigma_R(t) = \sqrt{(\sigma_R^0)^2 + (C_R/t)^2} \tag{4.15}$$

where t is the proper decay-time, and σ_L^0, C_L, σ_R^0, C_R are constants. Justification for the above parametrization is provided in Appendix A. In brief, the motivation for the above parametrization comes from the fact that the D^* width has two components. The first component comes from the multiple scattering of the slow pion from D^*, which is independent of D^0 decay-time. The second component comes from the uncertainty in the

D^0 direction of flight, which is smaller for longer lived decays. Thus the overall D^* width is smaller for longer lived D^0's. This is evident from Figures 4.2 and 4.3. These figures show the Q-value distributions in various decay-time ranges for the two decay modes in real data. It is clear that the D^* width gets narrower as the decay times get longer.

Parameters $Q_0, \sigma_L^0, C_L, \sigma_R^0$ and C_R used in equations 4.13 through 4.15 were determined from large RS signals in each decay mode during the fit.

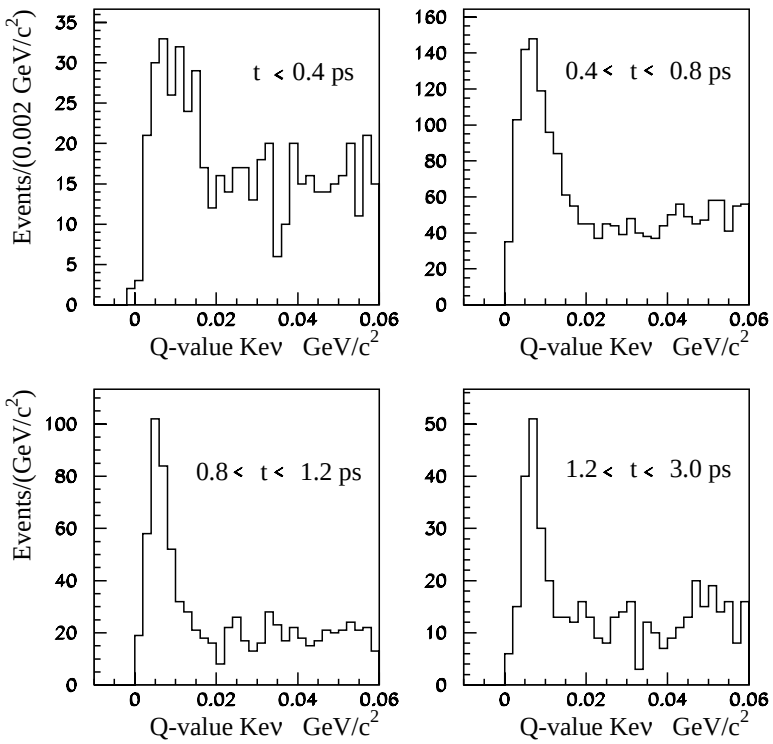

Figure 4.2: Q-value distribution for the $Ke\nu$ mode in different decay-time bins. The width of the D^* peak gets narrower as the decay-times get longer, as expected.

The function $f_b(Q)$, describing the background Q-value distribution, was obtained directly from the data by a process called *event-mixing* (not to be confused with $D^0 - \overline{D}^0$

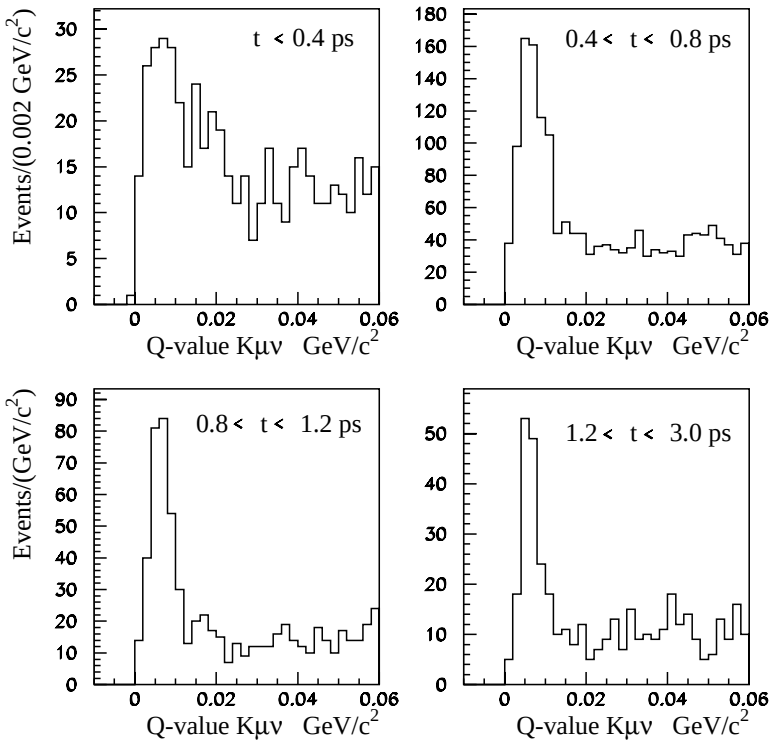

Figure 4.3: Q-value distribution for the $K\mu\nu$ mode in different decay-time bins. The width of the D^* peak gets narrower as the decay-times get longer, as expected.

mixing) in which a D^0 candidate from one event was combined with slow pions from 100 other events, and Q-value was calculated for each such combination. Each D^0 candidate was combined with 100 random pions in order to get a high statistics histogram, thus reducing the uncertainty in background shape in Q. The resulting Q-value distribution models D^0-random π as well as purely random combinatoric background, and provides a good representation of the shape of the background, as shown in Figure 4.1 (dashed lines). The dashed line in each histogram in Figure 4.1 is the Q-value distribution obtained from *event-mixing* and normalized to the number of events with $Q > 25$ MeV/c^2 (away from the signal region) in the respective solid-line histogram. Clearly, *event-mixing* provides a good model for the background shape. These *event-mixing* histograms were used directly to describe the background shapes bin-by-bin, appropriately normalized to give unity when integrated over the Q-value range of interest ($0 < Q < 60$ MeV/c^2).

Function $F_s^{MIX}(t)$ used to describe wrong-sign decay-time distribution was parametrized as:

$$F_s^{MIX}(t) = Bt^2(\epsilon(t)e^{-\Gamma t}) \tag{4.16}$$

where $\epsilon(t)$ is the detector acceptance as a function of decay-time t, and , $= 1/\tau_{D^0}$. B is a normalization factor such that the integral of this function over the whole time range is unity. Note that equation 4.16 describes the characteristic mixed decay-time distribution ($\propto t^2e^{-\Gamma t}$) modified by the detector acceptance ($\epsilon(t)$). The only unknown in the above equation is the detector acceptance function $\epsilon(t)$, which has to be obtained from data. Instead of obtaining this acceptance function separately, the function $\epsilon(t)e^{-\Gamma t}$ (the quantity in parentheses in equation 4.16) was obtained directly from the data. The decay-time distribution of the background-subtracted RS signal ($Q < 15$ MeV/c^2) events is proportional to $\epsilon(t)e^{-\Gamma t}$. These distributions are shown in Figures 4.4(a) and 4.4(b) for the $Ke\nu$ and $K\mu\nu$ modes respectively. By multiplying these distribution by t^2, the required mixed decay-time distribution (equation 4.16) is obtained. The histograms shown in Figures 4.4(a) and 4.4(b) were used directly during the fit, by multiplying the entry

in each bin by t^2, where t is the mean decay-time for that bin. The distribution was normalized to give unit integral over the decay-time range of interest ($0 < t < 3.0$ ps). This was done in order to normalize the likelihood function.

Function $F_b(t)$ describes the decay time distribution for the background events (both RS and WS), and it was obtained directly from data. The exact analytical form of this function is not known, but that is not necessary. This distribution is expected to be identical for both RS and WS background events (since the source of both are D^0-random π or purely random combinations of tracks). This expectation is validated by Figure 4.5 which shows that the decay-time distributions for both RS and WS sideband events are indeed identical within statistical errors. This shape was modeled by decay-time distributions of the events in the Q-value sideband ($0.025 < Q < 0.06$ GeV/c^2), as shown in Figures 4.4(c) and 4.4(d). Both RS and WS sideband events were used to model this shape in order to increase statistics. This is valid since only the events away from the signal region were used.

An implicit assumption involved in modeling the background decay-time distribution as described above is that the decay-time distribution is constant across different Q-value ranges. If this were not the case, the above-mentioned method would not be valid since the sideband distribution cannot be used to describe the decay-time distribution in all Q-value ranges (which is what is being done). In order to study any variation of the decay-time distribution across the Q-value spectrum, three slices (shaded areas in Figures 4.6(a) and 4.6(b)) of the Q-value sideband were chosen for each mode and the decay-time distribution for each slice was plotted as shown in Figures 4.6(c) and 4.6(d). Clearly, the decay-time distribution is constant within statistical errors as a function of Q-value. Therefore, the sideband decay-time distribution can be and was used to represent the decay-time distribution of background events in the whole Q-value range of interest.

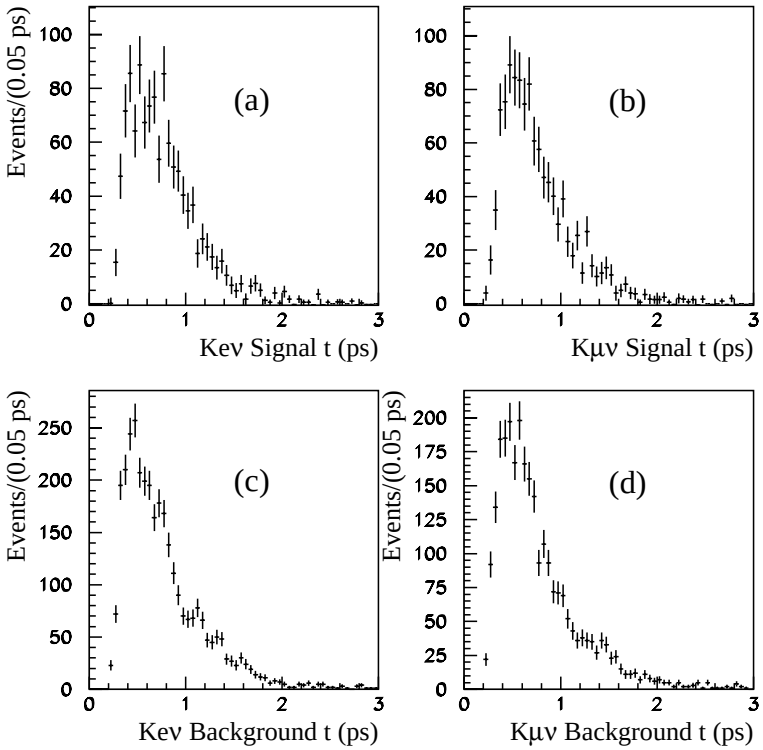

Figure 4.4: Decay-time distributions for the right-sign signal (a and b) and the background (c and d) for the $Ke\nu$ and $K\mu\nu$ modes. The background is from all possible sources. The distribution of the signal plots is proportional to $\epsilon(t)e^{-\Gamma t}$, where $\epsilon(t)$ is the detector acceptance as a function of the decay time. The exact analytical form of the background decay time distribution is not known, but that is not necessary. The histograms (c) and (d) were used directly to describe this distribution.

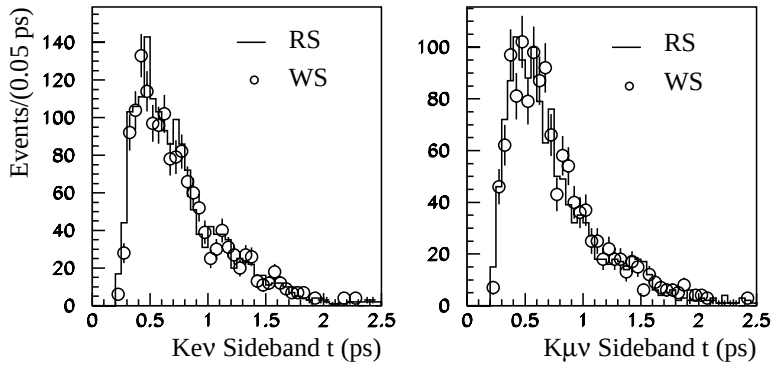

Figure 4.5: Comparison of the background decay-time distributions for right-sign (solid-line histograms) and wrong-sign (circles) events for $Ke\nu$ and $K\mu\nu$ modes from data. All these events are from the sideband region $0.025 < Q < 0.06$ GeV/c^2 in the Q-value plot. Clearly, the right- and wrong-sign decay-time distributions for background events are the same within statistical errors for both modes, as expected.

4.4 Fit Results

Final fit results were obtained by minimizing the negative log-likelihood function described in equation 4.8 (which is equivalent to maximizing the likelihood). The results of the fit are listed in Table 4.1. The fit finds 1237 ± 45 RS signal events in the $Ke\nu$ mode and 1267 ± 44 RS signal events in the $K\mu\nu$ mode. The number of mixed events is $N_{mix} = 4.4^{+11.8}_{-10.5}$ in the $Ke\nu$ mode and $N_{mix} = 1.8^{+12.1}_{-11.0}$ in the $K\mu\nu$ mode. Therefore, no evidence for $D^0 - \overline{D}^0$ mixing is found in either mode. The projections of the fit on Q-value distributions are shown in Figure 4.7. The mixing rate r and the 90% confidence level (C.L.) upper limit

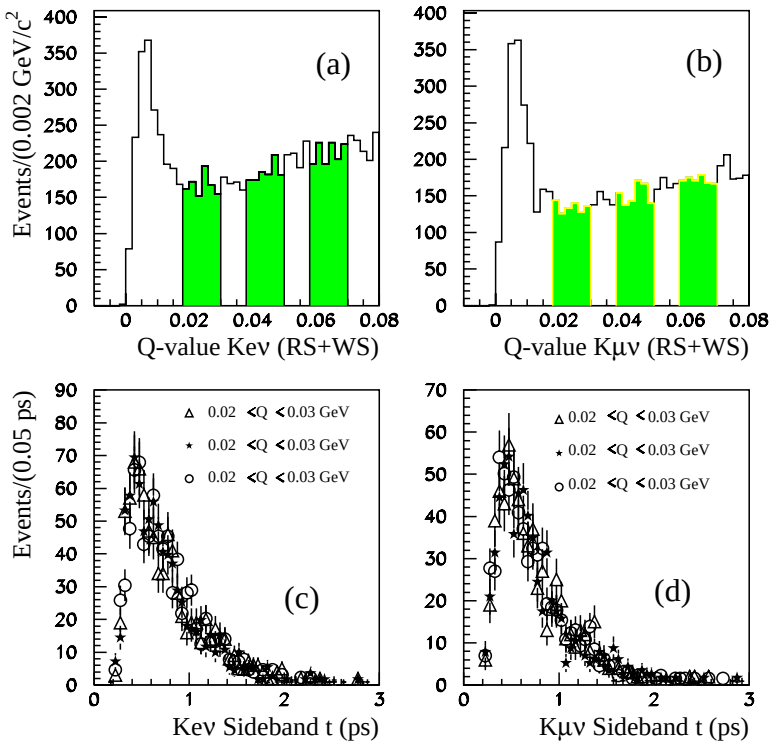

Figure 4.6: Decay time distributions for the events in various Q-value regions. The top two figures (a and b) show the three slices of the Q-value sideband that were chosen to study the variation of decay-time distribution. The bottom two figures (c and d) show the decay-time distributions for these Q-value slices. It is evident that the shape of the decay-time distribution is constant within statistical errors for different Q-value regions, so that it is justified to use the sidebands to represent the background decay-time distribution in the signal region.

on r are calculated in section 4.6.

Parameter Name	Fit Values for $Ke\nu$ data	Fit Values for $K\mu\nu$ data
Q_0	4.86 ± 0.30 MeV	5.17 ± 0.31 MeV
σ_L^0	1.98 ± 0.20 MeV	1.84 ± 0.25 MeV
C_L	0.00 ± 0.31 MeV-ps	0.78 ± 0.17 MeV-ps
σ_R^0	4.18 ± 0.44 MeV	3.51 ± 0.42 MeV
C_R	2.09 ± 0.29 MeV-ps	2.13 ± 0.24 MeV-ps
N_s^{RS}	1237 ± 45	1267 ± 44
N_b^{RS}	2395 ± 56	1889 ± 50
N_{mix}	$4.4^{+11.8}_{-10.5}$	$1.8^{+12.1}_{-11.0}$
N_b^{WS}	2278 ± 49	1935 ± 45

Table 4.1: Results from the maximum likelihood fit to the data

4.5 The Relative Correction Factor, α

In order to calculate the mixing rate from the fit values of N_s^{RS} and N_{mix}, one needs to know the correction factor that arises from different time-evolutions of the right-sign and mixing signals, and non-uniform acceptance of the detector as a function of proper decay time. of the D^0. Assuming there were a total of N_{RS}^0 right-sign decays, and N_{mix}^0 mixed decays produced in the experiment, the mixing rate would be:

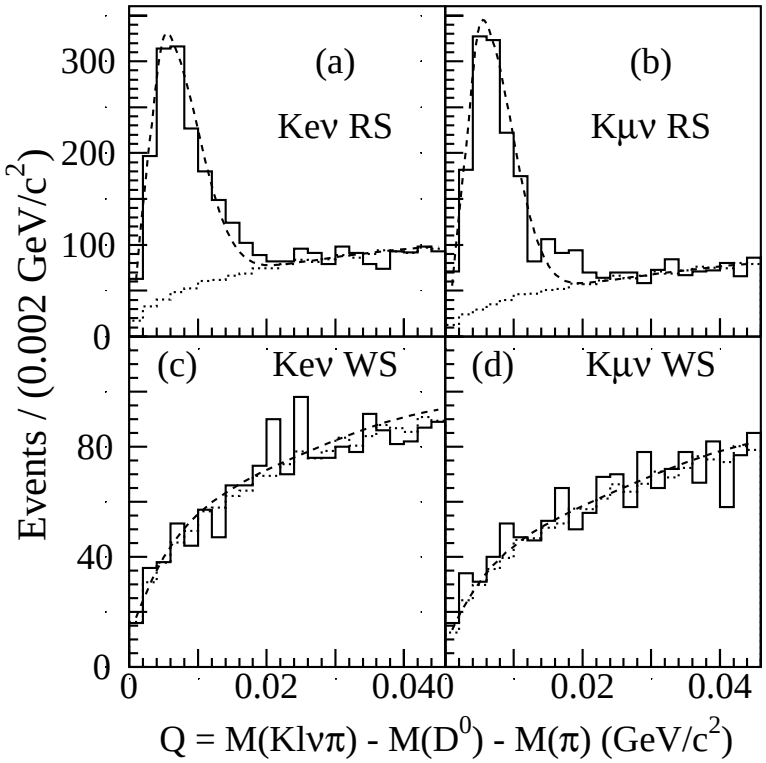

Figure 4.7: The Q-value distributions for (a) $Ke\nu$ RS, (b) $K\mu\nu$ RS, (c) $Ke\nu$ WS, and (d) $K\mu\nu$ WS candidates. The solid line histograms show the data Q-value distributions, the dashed lines are the projections of the fit in Q-value, and the dotted lines show the Q-value distribution obtained from combining a D^0 from one event and π from another (event mixing), normalized to the number of events with $Q > 0.025$ GeV/c^2 in the respective histograms.

$$r = \frac{N^0_{mix}}{N^0_{RS}} \tag{4.17}$$

But the number of decays observed in the experiment are:

$$N^{obs}_{RS} = N^0_{RS}, \int_0^\infty \epsilon(t) e^{-\Gamma t} dt \tag{4.18}$$

and,

$$N^{obs}_{mix} = N^0_{mix} \frac{1}{2}, {}^3 \int_0^\infty , \epsilon(t) t^2 e^{-\Gamma t} dt \tag{4.19}$$

where $\epsilon(t)$ is the detection efficiency as a function of decay time, and , is the width of D^0. The mixing rate now is,

$$r = \frac{N^0_{mix}}{N^0_{RS}} = \frac{N^{obs}_{mix}}{N^{obs}_{RS}} \times \frac{, \int_0^\infty \epsilon(t) e^{-\Gamma t} dt}{\frac{1}{2}, {}^3 \int_0^\infty \epsilon(t) t^2 e^{-\Gamma t} dt} \tag{4.20}$$

The above equation can be rewritten as:

$$r = \frac{N^{obs}_{mix}}{N^{obs}_{RS}} \times \alpha \tag{4.21}$$

where α is the correction factor:

$$\alpha \equiv \frac{, \int_0^\infty \epsilon(t) e^{-\Gamma t} dt}{\frac{1}{2}, {}^3 \int_0^\infty \epsilon(t) t^2 e^{-\Gamma t} dt} \tag{4.22}$$

Note that $\alpha \equiv 1$ if $\epsilon(t)$ is independent of t. The value of α is obtained from the background subtracted decay-time histogram of the right-sign signal events. This distribution is proportional to $\epsilon(t)e^{-\Gamma t}$, and can be used to evaluate the two integrals involved in the calculation of α. The integration was done bin-by-bin. The value of α for the two modes was found to be:

$$\alpha^{Ke\nu} = 0.44 \pm 0.02 \tag{4.23}$$

$$\alpha^{K\mu\nu} = 0.46 \pm 0.02 \tag{4.24}$$

The errors on $\alpha_{Ke\nu}$ and $\alpha_{K\mu\nu}$ arise from the fact that histograms with limited statistics were used to calculate their values. These errors were estimated by calculating the values of α for the two modes several times, while each time every bin in the decay-time distribution histograms was fluctuated independently and randomly by its bin error. The resulting values of α were plotted as a histogram as shown in Figure 4.8. The values of α calculated in this manner have an approximately Gaussian distribution, and the width of these Gaussians was taken as the error on α.

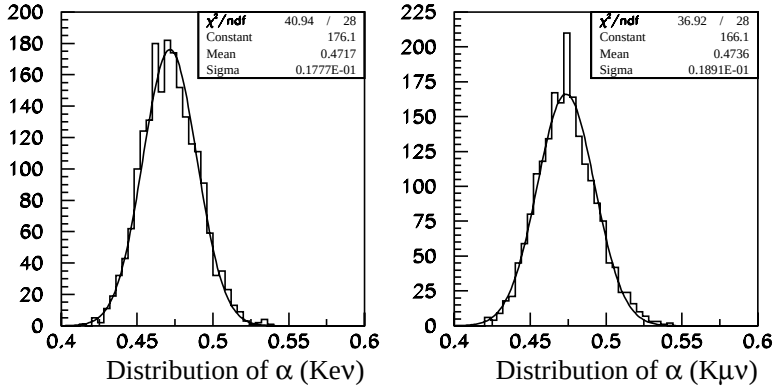

Figure 4.8: Distributions of the correction factor α as the individual time bins in the signal and background decay-time histograms are varied randomly and independently by their errors. The distributions are shown for both $Ke\nu$ and $K\mu\nu$ modes.

4.6 Calculation of the Mixing Rate

The mixing rates for the two modes, from equation 4.21 and the measured values of N_s^{RS} and N_{mix} (Table 4.1) and α (equations 4.24 and 4.24) are:

$$r_{Ke\nu} = \frac{4.4^{+11.8}_{-10.5}}{1237 \pm 45} \times (0.44 \pm 0.02) = 0.00156^{+0.0042}_{-0.0037} \tag{4.25}$$

or

$$r_{Ke\nu} = (0.16^{+0.42}_{-0.37})\% \tag{4.26}$$

Similarly for the $K\mu\nu$ mode:

$$r_{K\mu\nu} = \frac{1.8^{+12.1}_{-11.0}}{1267 \pm 44} \times (0.46 \pm 0.02) = 0.00065^{+0.0044}_{-0.0037} \tag{4.27}$$

or

$$r_{K\mu\nu} = (0.06^{+0.44}_{-0.40})\% \tag{4.28}$$

4.6.1 Combined Mixing Rate From the Two Modes

In order to compute the average mixing rate from the two modes, the PDG prescription of unconstrained weighted average [31] was used. Given various uncorrelated measurements $x_i \pm \delta x_i$ of the same quantity, the weighted average and the error is given by

$$\overline{x} \pm \overline{\delta x} = \frac{\sum_i w_i x_i}{\sum_i w_i} \pm (\sum_i w_i)^{-\frac{1}{2}} \tag{4.29}$$

where

$$w_i = \frac{1}{(\delta x_i)^2} \tag{4.30}$$

The $Ke\nu$ and $K\mu\nu$ data samples are statistically independent, and the mixing rates obtained from the two samples are expected to be uncorrelated. Using the above prescription, the combined mixing rate is:

$$r = (0.11^{+0.30}_{-0.27})\% \tag{4.31}$$

This gives an upper limit for $D^0 - \overline{D}^0$ mixing of:

$$r < 0.50\% \text{ @ } 90\% \text{ C.L.} \tag{4.32}$$

This upper limit corresponds to the point where the log-likelihood changes by 0.82, i.e., $\Delta \ln L = 0.82$ [32].

It is instructive to examine the decay-time distribution of the WS events in the signal region ($Q < 0.015$ GeV/c^2), as shown in Figure 4.9. The crosses show the WS data decay-time distribution. The dotted line shows the expected D^0 (unmixed) decay-time distribution uncorrected for detector acceptance, normalized to the number of events with $t > 0.7$ ps (where acceptance is uniform). The dashed line represents the expected decay-time distribution uncorrected for detector acceptance for a mixing signal corresponding to the 90% C.L. limit obtained in this analysis for each mode. Clearly, all the WS events in the signal region appear to be consistent with unmixed D^0 decay-time distribution, and not with mixing, as predicted by the fit.

4.7 Some Systematic Checks

Since right- and wrong-sign data samples were selected using identical selection criteria, most systematic uncertainties cancel in the mixing rate. However, some possibly significant

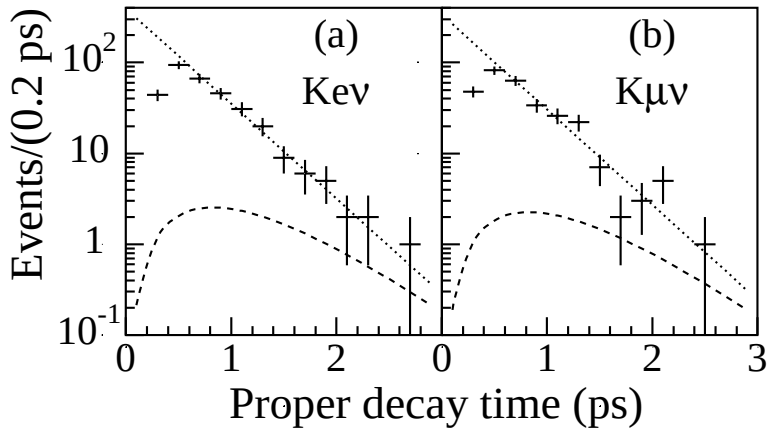

Figure 4.9: The decay-time distribution of the wrong-sign events in the signal region ($Q <$ 15 MeV) for the $Ke\nu$ (a) and the $K\mu\nu$ (b) modes. Crosses represent the measured decay-time distributions, and the dotted line shows the expected D^0 decay-time distribution uncorrected for detector acceptance, normalized to number of events with $t > 0.7$ ps (where acceptance is uniform). The dotted line represents the expected decay-time distribution uncorrected for detector acceptance for $Ke\nu$ and $K\mu\nu$ mixing signals corresponding to our 90% C.L. limit in each mode.

sources of systematic error remain. These systematic errors could come from hadronic feedthrough into the semileptonic sample, smearing in decay-time distribution or any possible bias in the fitting procedure. These possible sources of systematic uncertainty and their effect on the mixing rate are discussed in this section.

4.7.1 Effect of Hadronic Feedthrough

Throughout this analysis, it was implicitly assumed that the data sample used for this analysis is purely semileptonic, that there is no hadronic feedthrough. In real life though, there is always a small hadronic feedthrough, both in RS and WS samples. An approximate estimate of the effect of this feedthrough on the mixing rate can be obtained as described below.

If there were no hadronic feedthrough, the events we see would be purely semileptonic, and the correct mixing rate would be:

$$r = \frac{N_{SL}^{mix}}{N_{SL}^{RS}} \tag{4.33}$$

where the subscript SL signifies that these are purely semileptonic events. It has been assumed that the correction factor $\alpha = 1$ for simplicity. Since α is an overall scale factor, the conclusions reached here are independent of the exact value of α.

Since there is always a small hadronic feedthrough in the experimental data sample, the measured mixing rate r' is:

$$r' = \frac{N_{SL}^{RS} + N_{had}^{RS}}{N_{SL}^{mix} + N_{had}^{WS}} \tag{4.34}$$

where subscript *had* refers to the hadronic feedthrough into the semileptonic sample. For example, N_{SL}^{RS} is the true number of semileptonic right-sign events, and N_{had}^{RS} is the number of right-sign hadronic events feeding into the right-sign sample, and so on. This equation can be re-written as:

$$r' = \frac{r + x}{1 + y} \tag{4.35}$$

where r is the true mixing rate defined in equation 4.33, $x = (N_{had}^{WS}/N_{SL}^{RS})$, and $y = (N_{had}^{RS}/N_{SL}^{RS})$. Both x and y are much smaller than 1. One can express the true mixing rate r in terms of the measured mixed rate r':

$$r = (1 + y)r' - x \tag{4.36}$$

In the above equation, x represents the amount of hadronic feedthrough in the wrong-sign data sample. It is expected to be small, since double misidentification is required for a hadronic decay such as $D^0 \to K^-\pi^+\pi^0$ to end up in the wrong-sign data sample. This would happen if the kaon is misidentified as a lepton and the pion is misidentified as a kaon. The probability for this double misidentification is $(0.11 \pm 0.10)\%$ into the $Ke\nu$ mode and $(0.61 \pm 0.02)\%$ into the $K\mu\nu$ mode. Monte Carlo studies indicate less than 10 events of this kind are expected in the WS signal region in each mode, which is much less than the number of combinatoric background events present, and therefore this effect was ignored. This is conservative, since correcting for this effect would result in a mixing rate lower than the measured one, thus lowering the upper limit being set in this analysis.

The hadronic feedthrough into the right-sign data sample, represented by y in equation 4.36, mainly comes from decays such as $D^0 \to K^-\pi^+\pi^0$, in which the kaon is identified correctly and the charged pion is misidentified as a lepton, while the neutral pion simulates the kinematics of the neutrino. The decay mode $D^0 \to K^-\pi^+$ was explicitly removed by applying a mass cut in both RS and WS data samples, as described in Chapter 3. The amount of feedthrough from the $K^-\pi^+\pi^0$ and $K^-\pi^+\pi^0\pi^0$ decay modes was estimated by Monte Carlo simulations. The total number of such events feeding into the RS signal from both modes is expected to be approximately 3% of the RS signal in $Ke\nu$ and $K\mu\nu$ modes each, i.e., $y \sim 0.03$. This is small effect, of the order of statistical errors on N_{RS} in each mode, and was ignored. As discussed in section 4.7.5, the analysis systematically overestimates the mixing rate by approximately 10%, so that ignoring this small effect does not result in underestimating the upper limit.

4.7.2 Effect of Smearing in Signal Decay-Time Distribution

It has been assumed in this analysis that the decay-time distribution of mixed events is described by equation 4.16, i.e., it is proportional to $t^2\epsilon(t)e^{-\Gamma t}$. This is only true in the ideal case when the decay time is measured accurately without any error. Because of finite resolution of the detector and the choice of the one of the two neutrino momentum solutions, the measured decay-time distribution differs slightly from the distribution used in the fit. The method used to estimate the effect of this smearing in decay time on the mixing rate is described below.

First, the amount of smearing in measured decay times was estimated from Monte Carlo simulations by comparing the true and reconstructed decay times, after applying all the analysis cuts. This was done for both the $Ke\nu$ and $K\mu\nu$ modes in different decay-time ranges and results are shown in Figures 4.10 and 4.11. A Gaussian was fit to each smearing distribution and the σ of the Gaussian was taken as the smearing in that particular decay-time region.

The detector efficiency function is also required for this test. It was obtained from Monte Carlo, using the true decay-time distribution for all the events that passed the final analysis cuts (Figure 4.12). The efficiency function was parametrized as:

$$\epsilon(t) = \begin{cases} 0 & \text{if } t < 0.2 \text{ ps} \\ P1 + P2 * t & \text{if } 0.2 \leq t < P3 \\ P1 + P2 * P3 & \text{if } t \geq P3 \end{cases} \tag{4.37}$$

where *P1,P2*, and *P3* are parameters obtained from the fit to the MC events. The shape of this function, and the values of the parameters involved are shown in Figure 4.12.

Once the smearing and the acceptance functions were known, mixed and exponential decay-time distributions using measured smearing and acceptance functions were generated. The resulting distributions are shown in Figure 4.13.

In order to estimate the effect of this smearing in decay times on the determination

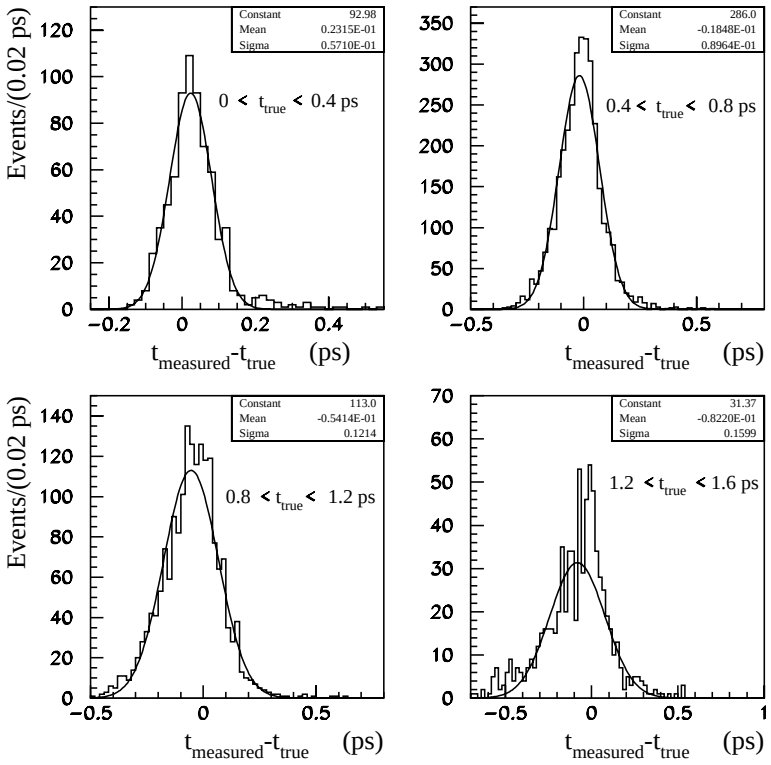

Figure 4.10: Smearing distributions in different time bins for the $Ke\nu$ mode. The quantity plotted is $\delta t \equiv t_{measured} - t_{true}$. A Gaussian fit was performed on the distributions, and the fit values were used to generate high-statistics smeared exponential and mixed decay-time distributions to study the effect of smearing on the mixing limit.

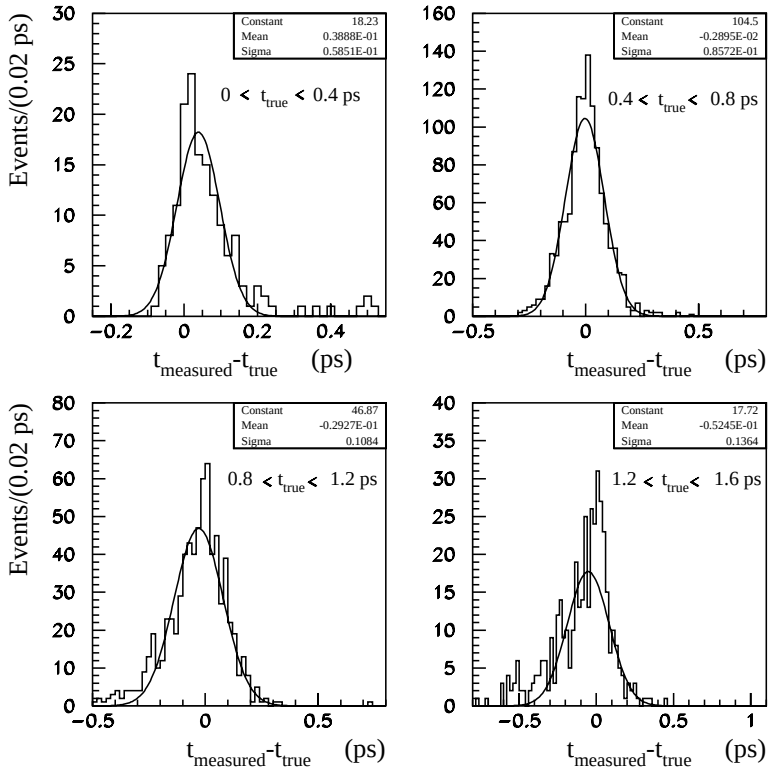

Figure 4.11: Smearing distributions in different time bins for the $K\mu\nu$ mode. The quantity plotted is $\delta t \equiv t_{measured} - t_{true}$. A Gaussian fit was performed on the distributions, and the fit values were used to generate high-statistics smeared exponential and mixed decay-time distributions to study the effect of smearing on the mixing limit.

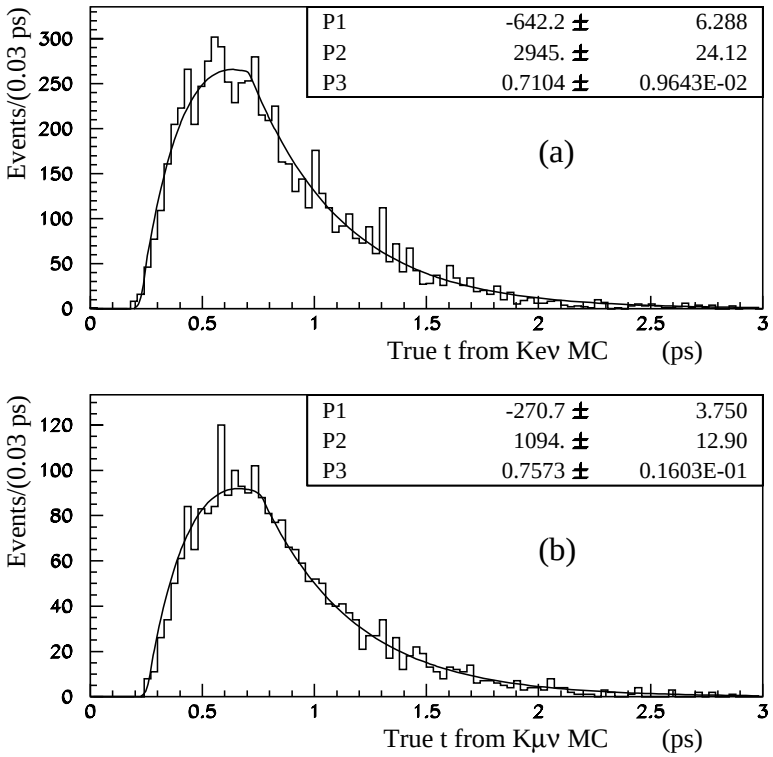

Figure 4.12: True decay-time distributions for the $Ke\nu$ and $K\mu\nu$ MC events that passed all final analysis cuts. The shape of the acceptance curve obtained from the fit was used to generate high-statistics mixed and exponential decay-time distributions to study the effect of smearing on the mixing limit.

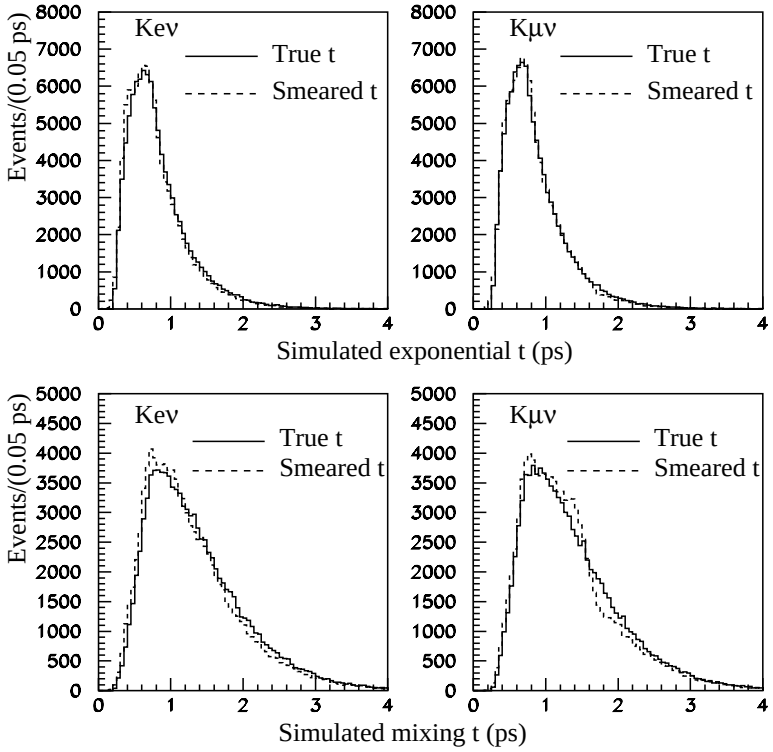

Figure 4.13: Simulated exponential and mixed decay-time distributions for the $Ke\nu$ and $K\mu\nu$ modes. The solid-line histogram is the unsmeared, and the dashed histogram is the smeared, distribution in all plots. It is clear that the smeared and unsmeared distributions are not very different, suggesting that the effect of smearing on the mixing limit is small.

of mixing rate, two different fits were performed to the data, as described below, and the results from the two fits were compared. The difference between the two results is a measure of the uncertainty introduced due to the smearing in decay time, t.

In the first method, referred to as the *Data Method*, an acceptance-modified and properly-smeared exponential D^0 decay-time distribution was generated as described above. This decay-time distribution was then used in the maximum likelihood fit instead of the one obtained from data (keeping all other distributions as before, obtained directly from data), and the fit performed. This is equivalent to the data fit, except that the right-sign signal decay-time distribution obtained from data has been replaced by a high-statistics simulated exponential. The mixing decay-time distribution is now obtained by multiplying this simulated exponential distribution by t^2.

In the second method, referred to as the *Ideal Method*, both exponential *and* mixing decay-time distributions were generated separately, with appropriate smearing and acceptance modification. Now, instead of multiplying the right-sign decay-time distribution by t^2 to obtain the mixed distribution, as was done in the data, the mixed decay-time distribution was obtained directly from the simulated mixed decay-time histogram. The right-sign decay-time distribution was obtained from the simulated exponential. This is the correct way to obtain the right- and wrong sign decay-time distributions. The reason this method cannot be used in real data is that no natural mixing sample exists that can be used to model the mixing decay-time distribution, and the use of Monte Carlo was intentionally avoided in the analysis to make it self contained (MC was only used to estimate systematic effects).

Now, if the fits are done to a given data set using the *Data Method* and the *Ideal Method*, the difference between the values of N_{mix} obtained from the two methods would be a measure of the uncertainty in N_{mix} due to the smearing in decay-time distribution. This technique was used to estimate the systematic error on N_{mix} due to smearing of the decay time. Maximum-likelihood fits were performed to both the $Ke\nu$ and the $K\mu\nu$ data sets using the two methods described above, for various values of the smearing; the results

are shown in Table 4.2.

Amount of smearing	$Ke\nu$ mode			$K\mu\nu$ mode		
	N_1	N_2	$\Delta N = N_1 - N_2$	N_1	N_2	$\Delta N = N_1 - N_2$
0σ	7.7	7.3	0.4	-3.3	-3.1	-0.2
1σ	7.3	8.2	-0.94	-3.2	-4.4	1.2
2σ	5.6	7.0	-1.4	-4.4	-5.1	0.7
3σ	4.3	5.1	-0.8	-3.8	-3.6	0.2

Table 4.2: Effect of smearing in decay time on N_{mix}. $N_1 = N_{mix}$ from the *Ideal Method*, $N_2 = N_{mix}$ from the *Data Method*. Meanings of the Data Method and Ideal Method are described in the text. σ = width of the Gaussian smearing function.

The first row in the Table 4.2 shows the results when fits were done with *no* smearing. This was done to see if there is any difference in the results due to the two different methods. In the absence of smearing, the two methods are equivalent and the two answers should not be different. Indeed the answers obtained by the two methods in the absence of smearing are nearly identical for both modes.

The second row in Table 4.2 (with 1σ smearing) shows the change in the fit results due to smearing. The value of ΔN is small for both modes, compared to the statistical errors. This ΔN is the systematic error in N_{mix} due to smearing in decay time.

The third and fourth rows show the results for 2σ and 3σ (twice and three times as much) smearing respectively. Again the value of ΔN is small for both modes. These fits were done to check whether ΔN changes appreciably as the smearing is increased.

It can be concluded from this study that the effect of smearing on the fit results is negligible. This is not surprising, since Figure 4.13 shows that the unsmeared and smeared distributions do not differ much for either the exponential or mixed cases. Therefore, the effect of smearing on mixing limit was ignored in this analysis.

4.7.3 Test of the Sensitivity of the Fit to a Small Mixing Signal

It is important to check whether the fitting procedure used in this analysis can find a small mixing signal if any were present in the data sample. This check was done using two methods, as described below. The objective of this study was to check for any errors or biases in the analysis technique.

In the first test, four different Monte Carlo samples with a known amount of mixing (0.5%, 1.0%, 1.5% and 2%) were generated and then put through all the processes and selection criteria that were applied to real data. A fit, identical to the one used in the real analysis, was done to each resulting final Monte Carlo sample in order to extract the mixing rate. Since the mixing rates in these samples are known, the fit values can be compared with the true values. The results of this study are shown in Table 4.3.

It is clear from Table 4.3 that the fit results are consistent with the input values within error bars.

In another test to check for biases in the fitting procedure, a large sample of pure mixing Monte Carlo was generated and made to pass through all the steps and selection criteria as in real data. A fixed number of events from this mixed Monte Carlo were added to the real wrong-sign data sample, keeping the right-sign data sample unchanged. Then the usual fit was performed on this sample. All the quantities in this fit are from real data except for a known number of mixed MC events that were added. The fit was repeated several times for a given fixed number of Monte Carlo events, and statistically independent samples of MC were used in each fit. The mean output from these fits was recorded. The sample sizes used were 10, 20, 30, and 40 events (error on N_{mix} is of the order of 10).

Results of Fits to MC Mixing Signals		
	Mixing Rate From the Fit	
Generated Mixing	$Ke\nu$ Mode	$K\mu\nu$ mode
0.5%	$(0.49 \pm 0.11)\%$	$(0.71 \pm 0.14)\%$
1.0%	$(0.74 \pm 0.13)\%$	$(1.22 \pm 0.17)\%$
1.5%	$(1.35 \pm 0.17)\%$	$(1.70 \pm 0.19)\%$
2.0%	$(1.86 \pm 0.19)\%$	$(2.53 \pm 0.22)\%$

Table 4.3: Results of various fits to MC samples with known amounts of mixing

The results are shown in Table 4.4. One can again conclude from this table that the fit finds the correct number of mixed events within statistical error bars, validating the fitting procedure.

4.7.4 Test of the Method to Calculate α

In order to calculate the mixing rate from the fit numbers, the relative correction factor α that arises from different time evolutions of the mixed and unmixed decays must be calculated. In this analysis, α was calculated directly from the background-subtracted decay-time histogram of right-sign signal using numerical integration.

A test was done to check the accuracy of this method. This was done by generating a high-statistics decay-time histogram using raw Monte Carlo sample in which the true decay time for each D^0 is known. Since no selection criteria are applied, the acceptance is independent of the decay-time for these events and is constant. Now if the numerical

integration method is used to calculate α for this distribution, one must get $\alpha = 1$ if the method is correct. In addition, one can artificially cut off the acceptance below a certain t_0 and use a simplistic model for the detector efficiency such that $\epsilon(t) = 0$ for $t < t_0$ and $\epsilon(t) = 1$ otherwise. In such a model, α can be calculated analytically. This analytical result can be compared with the result obtained by numerical integration. If the method is correct, the two results must agree. The values of α for these cases were calculated analytically as well as numerically (as in the analysis). The results are listed in Table 4.5. It is clear from this table that the numerical integration method used in this analysis is correct, since it gives values of α that are in agreement with analytical calculations.

4.7.5 Check for Bias in α due to the Choice of Neutrino Momentum

A test was done to look for bias in α introduced by the choice of the positive solution for neutrino momentum in the analysis. This was done by calculating α from two different Monte Carlo decay-time histograms, after applying all the analysis cuts. In the first method, α was calculated using the true decay-time histogram, and in the second method, using the one obtained from the positive neutrino momentum solution. The results are listed in Table 4.6. This table shows that the value of α is overestimated by approximately 10% as a result of choosing the positive neutrino momentum solution. Since α is an overall correction factor, the effect of this bias is to overestimate the mixing rate r by approximately 10%. Since an upper limit is being set in this analysis, it was conservatively decided not to correct for this systematic overestimate.

4.7.6 Summary of Systematic Checks

Various tests done to study systematic effects in the analysis indicate that they are not large. The overall fit tends to overestimate the mixing rate by 10%. No correction was made for this effect, which results in a more conservative upper limit on $D^0 - \overline{D}^0$ mixing rate.

Test of the Fitting Procedure			
$Ke\nu$ mode			
		Fit Results	
N_{in}	Number of fits	N_{out}	Mean σ_N
10	40	13.9	12.0
20	40	24.8	12.7
30	40	33.3	13.3
40	40	43.5	13.8
$K\mu\nu$ mode			
		Fit Results	
N_{in}	Number of fits	N_{out}	Mean σ_N
10	36	13.5	12.1
20	36	26.7	12.7
30	36	37.0	13.3
40	36	48.7	13.8

Table 4.4: Results of the fit when a known fixed number of mixed MC events were thrown in WS data. N_{in} is the number of mixed MC events included. Several fits were done with statistically independent mixed MC samples of a given size to obtain a mean output. N_{out} is the mean number of mixed events found by the fit. σ_N is the mean statistical error on N_{out} as obtained by the fit.

t_0	α from numerical integration	α from analytic calculation
0.0	(1.02 ± 0.009)	1.00
0.2	(0.65 ± 0.006)	0.62
0.3	(0.52 ± 0.004)	0.50
0.4	(0.43 ± 0.004)	0.41

Table 4.5: Test of the method used to calculate α.

Values of α from true and measured t		
	Using true t	Using measured t
$Ke\nu$ mode	0.40 ± 0.007	0.44 ± 0.008
$K\mu\nu$ mode	0.42 ± 0.008	0.45 ± 0.009

Table 4.6: Values of α from Monte Carlo using true and measured proper decay-time.

Chapter 5

Final Results and Conclusion

5.1 Introduction

The final results obtained from this analysis and a discussion of other experimental results are presented in this section.

5.2 Final Results

The analysis presented in this thesis is the first search for $D^0 - \overline{D}^0$ mixing using reconstructed semileptonic decays in both $Ke\nu$ and $K\mu\nu$ modes. The mixing search was performed by looking for $D^{*+} \to \pi^+ D^0 \to \pi^+ \overline{D}^0 \to \pi^+ (K^+ l^- \bar{\nu}_l)$ candidates with decay-time information characteristic of mixing. There is no doubly Cabibbo suppressed (DCS) amplitude in semileptonic decays, so that the problems of DCS background and the interference between DCS and mixing amplitudes do not exist in this analysis, making the interpretation of the results straightforward.

Large and clean signals were found in the right-sign samples. An unbinned maximum likelihood fit was was performed to the data using Q-value and proper-decay time t in order to extract any mixing signal. There are 1237 ± 45 RS signal events in the $Ke\nu$

mode and 1267 ± 44 RS signal events in the $K\mu\nu$ mode. The number of mixed events are $4.4^{+11.8}_{-10.5}$ in the $Ke\nu$ mode and $1.8^{+12.1}_{-11.0}$ in the $K\mu\nu$ mode. The mixing rates from the two modes are measured to be:

$$r_{Ke\nu} = (0.16^{+0.42}_{-0.37})\% \tag{5.1}$$

$$r_{K\mu\nu} = (0.06^{+0.44}_{-0.40})\% \tag{5.2}$$

The average mixing rate from these two statistically-independent results is:

$$r = (0.11^{+0.30}_{-0.27})\% \tag{5.3}$$

This gives an upper limit on $D^0 - \overline{D}^0$ mixing rate of:

$$r < 0.50\% \text{ @ } 90\% \text{ C.L.} \tag{5.4}$$

This is the best model independent limit on $D^0 - \overline{D}^0$ mixing to date.

5.3 A Survey of Previous $D^0 - \overline{D}^0$ Mixing Measurements

In this section some of the more recent searches for $D^0 - \overline{D}^0$ mixing and their limitations are described. Earlier searches for $D^0 - \overline{D}^0$ mixing, not discussed here, can be found in references 33 and 34. A good review of the current status and future prospects of $D^0 - \overline{D}^0$ mixing search can be found in reference 35.

5.3.1 Fermilab E691

Fermilab experiment E691 [36] studied $D^0 - \overline{D}^0$ mixing by looking for the decay chain $D^{*+} \to \pi^+ D^0$, followed by $D^0 \to \overline{D}^0 \to K^+ \pi^-$ or $K^+\pi^-\pi^+\pi^-$. A wrong-sign charged K from the neutral D decay (*e.g.*, $D^0 \to \overline{D}^0 \to K^+\pi^-$) can be a signature of mixing.

However, a wrong-sign K can also come from doubly-Cabibbo-suppressed (DCS) decays in which a D^0 decays directly into a wrong-sign kaon ($e.g., D^0 \to K^+\pi^-$). Moreover, the DCS amplitude can interfere with the mixing amplitude, reducing the sensitivity to mixing, even though the mixing, DCS, and interference terms in principle can be separated statistically with decay time information. E691 reported a 90% confidence level (C.L.) upper limit on $D^0 - \overline{D}^0$ mixing of $r < 0.37\%$ assuming no interference between DCS and mixing amplitudes. If interference is allowed, their limit varies in the range (0.4 to 0.7)% in the $K\pi\pi\pi$ mode and from (0.5 to 1.9)% in the $K\pi$ mode, depending on the value of the interference term allowed. Thus, the result from E691 depends on how the interference term is treated in the fit.

5.3.2 Fermilab E615

Fermilab experiment E615 [37] searched for mixing by looking for pairs of muons with the same charge in a single event. Same-sign muons could come from the semileptonic decay of a D meson (D^0 or D^+) and a $\overline{D}^0$ that has oscillated into a D^0. E615 obtained a 90% confidence level upper limit on $D^0 - \overline{D}^0$ mixing of $r < 0.56\%$ using specific assumptions for charm production cross sections and D branching fractions. They assumed that the charm production cross section is proportional to the first power of the atomic number of the target, i.e., $\sigma_{c\bar{c}} \propto A^1$. Since a tungsten target was used, the limit could grow by a factor of two if instead the the cross section dependence were $A^{0.9}$. Thus, the result from E615 is again model-dependent.

5.3.3 CLEO II

More recently, CLEO II [38] has observed a wrong-sign signal in the mode $D \to K\pi$. They measured the ratio of the wrong-sign to right-sign decays to be $(0.77 \pm 0.25 \pm 0.25)\%$. Since they did not have decay time information for this measurement, they cannot differentiate between mixing and DCS decays, so that there is no way to unambiguously interpret these

numbers. This wrong-sign signal could be a result of mixing, DCS or a combined effect of the two. But this measurement from CLEO II makes the mixing search very interesting, since if this signal is from mixing it would be a clear indication of new physics.

5.3.4 Fermilab E791, Hadronic Analysis

The E791 collaboration pursued $D^0 - \overline{D}^0$ mixing search using large sample of hadronic D^0 decays $D^0 \to K^-\pi^+$ and $D^0 \to K^-\pi^+\pi^-\pi^+$ [39]. Approximately 5600 RS events in the $K\pi$ mode and 3400 RS events in the $K\pi\pi\pi$ mode were observed, with small backgrounds. The analysis was done with a variety of assumptions. In the most general case, CP violation was allowed and the fits were done to D^0 and $\overline{D}^0$ samples separately, also allowing for interference between DCS and mixing amplitudes. The mixing rates obtained for this case are:

$$\begin{aligned} r(D^0 \to \overline{D}^0) &= (0.70^{+0.58}_{-0.53} \pm 0.18)\% \\ r(\overline{D}^0 \to D^0) &= (0.18^{+0.43}_{-0.39} \pm 0.17)\% \end{aligned} \tag{5.5}$$

When no CP violation and no interference is allowed, the value of mixing rate from the hadronic analysis is:

$$r = (0.21^{+0.09}_{-0.09} \pm 0.02)\% \tag{5.6}$$

By comparing equations 5.5 and 5.6, the drastic effect of the assumptions made in the fit on the final results is clear. Even though both results are consistent with no mixing, the statistical error bars in equation 5.6 are almost four times smaller than those in equation 5.5. This reduction in error bars comes mainly from the assumption that there is no interference between DCS and mixing amplitude.

Therefore, the hadronic mixing analysis demonstrates that the final results are very sensitive to the assumptions made in the fit about the interference term. Treating the

interference term correctly adds more unconstrained parameters, weakening the sensitivity of the fit considerably. That is why the results from the hadronic analysis are comparable to the semileptonic results, despite cleaner and bigger signals. In hadronic analysis, there are a total of approximately 9000 events in the right-sign signal as opposed to only about 2500 signal events in the semileptonic modes. The presence of higher background and fewer events in the semileptonic modes are compensated by the fact that the fitting function is much simpler, since there is no DCS amplitude.

5.4 Conclusion

For the first time, a search for $D^0 - \overline{D}^0$ mixing has been performed using reconstructed semileptonic decays, together with decay-time information. This analysis not only demonstrates the feasibility of using semileptonic decays to search for mixing, but also sets the best model independent upper limit on $D^0 - \overline{D}^0$ mixing to date.

Future fixed-target experiments, such as Fermilab E831 (FOCUS) can use this technique to search for $D^0 - \overline{D}^0$ mixing with greater sensitivity. In fact, the E791 hadronic mixing analysis [39] demonstrates that the advantage of large and clean signals in hadronic decay modes are overshadowed by the presence of DCS background, so that the final sensitivity in these decays is worse that what can be expected from statistics alone. Therefore, the analysis presented here is one of the most promising way of searching $D^0 - \overline{D}^0$ mixing in the future. Fermilab experiment E831 is currently running, and expects to have 10^6 fully reconstructed charm decays (in comparison, E791 reconstructed approximately 150,000 charm decays). With such high statistics and good lepton identification, E831 can use this technique to search for $D^0 - \overline{D}^0$ mixing to a much greater sensitivity. CLEO II has installed a vertex detector, and they have an excellent electron identification system. With this vertex detector, they can also use this technique.

This technique is also useful in collider experiments. It can be used in conjunction with another method that uses quantum statistics of the production and decay of a $D^0\ \overline{D}^0$

pair in order to enhance statistics. The method of quantum statistics [40] can only be applied to the cases where a $D^0\ \overline{D}^0$ pair is produced in a state of odd orbital angular momentum, but the semileptonic method can be applied to any event where at least one D^0 is produced. For example, if a $D^- D^{*+}$ pair is produced, the the semileptonic method can be applied to the D^* decay, while the D^- tagging can be used to reduce background.

The limit set by this analysis is still several orders of magnitude away from the Standard Model predictions. This leaves a large window for new physics exploration, so that search for $D^0 - \overline{D}^0$ mixing remains an exciting endeavor for future charm experiments. This is especially true in the light of CLEO II observation [38] of a wrong-sign signal, which could be either from $D^0 - \overline{D}^0$ mixing or doubly Cabibbo suppressed decays, or a combined effect of both. The technique used in this analysis can be successfully employed to resolve this question.

Bibliography

[1] A. Datta and D. Kumbhakar, Zeit. für Phys. **C27**, 515 (1985).

[2] J. F. Donoghue *et al.*, Phys. Rev. **D33**, 179 (1986).

[3] L. Wolfenstein, Phys. Lett. **B164**, 170 (1985).

[4] H. Georgi, Phys. Lett. **B297**, 353 (1992).

[5] T. Ohl, G. Ricciardi and E. H. Simmons, Nucl. Phys. **B403**, 605 (1993).

[6] G. Burdman, *Charm Mixing and CP Violation in the Standard Model*, in Proceedings of the CHARM2000 Workshop, Fermilab, June 7-9, 1994.

[7] J. L. Hewett, *Searching for New Physics with Charm*, hep-ph/9505246, Proceedings of the LAFEX International School on High Energy Physics, LISHEP95, Feb 6-22, 1995, Rio de Janeiro, Brazil.

[8] L. Oliver, *Mixing and CP Violation in D Mesons*, talk delivered at the Journees sur les projects de Physique Hadronique, Societe Francaise de Physique, Super-Besse (France), 12-14 Jan, 1995.

[9] S. Pakvasa and H. Sugawara, Phys. Lett. **B73**, 61 (1978).

[10] T. P. Cheng and M. Sher, Phys. Rev. **D35**, 3484 (1987).

[11] L. Hall and S. Weinberg, Phys. Rev. **D48**, 979 (1993).

[12] K. S. Babu *et al.*, Phys. Lett. **B205**, 540 (1988).

[13] S. Davidson, D. Bailey and B. A. Campbell, Z. Phys. **C61**, 613 (1994).

[14] M. Leurer, Phys. Rev. Lett. **71**, 1324 (1993); Phys. Rev. **D48**, 333 (1994).

[15] M. Leurer, Y. Nir and N. Seiberg, Nucl. Phys. **B420**, 468 (1994).

[16] Y. Nir and N. Seiberg, Phys. Lett. **B309**, 337 (1993).

[17] L. F. Abbot, P. Sikivie and M. B. Wise, Phys. Rev. **D21**, 1393 (1980).

[18] V. Barger, J. L. Hewett and R. J. N. Phillips, Phys. Rev. **D41**, 3421 (1990).

[19] Y. Grossman, Nucl. Phys. **B426**, 355 (1994).

[20] G. Blaylock, A. Seiden and Y. Nir, Phys. Lett. **B355**, 555 (1995).

[21] *Performance of the Cerenkov Counters in the Fermilab Tagged Photon Spectrometer Facility*, D. Bartlett *et al.*, Nucl. Instr. Meth. **A260** 55 (1987).

[22] *A large area liquid scintillation multiphoton detector*, V. K. Bharadwaj *etal.*, Nucl. Instr. **228** 283 (1985).

[23] *Hadron Calorimetry at the Fermilab Tagged Photon Spectrometer Facility*, J. A. Appel *et al.*, Nucl. Instr. Meth. **A243** 361 (1986).

[24] *Description of Analysis of Muon Wall Efficiency*, N. Witchey, A. Nguyen and N. W. Reay, E791 offline document number 113.

[25] *Search for Flavor Changing Neutral Current Decays of Charm Mesons*, Ph. D. Thesis, N. J. Witchey, The Ohio State University, 1996.

[26] S. Amato *et al.*, Nucl. Instr. Meth. **A324** 535 (1993).

[27] *A Search for $D^0 - \overline{D}^0$ Mixing in Semileptonic Modes*, A. Tripathi, E791 offline document number 199.

[28] *Cerenkov Software*, L. Cremaldi, E791 offline document number 44.

[29] *Electron Identification in the E791 Offline Reconstruction Code*, P. Gagnon, P. Burchat, and P. Kasper, E791 offline document number 88.

[30] *Measurements of The Form Factors in the Semileptonic Decay* $D^+ \to \bar{K}^{*0} e^+ \nu_e$, Ph. D. Thesis, P. Gagnon, SCIPP 93/47, UC Santa Cruz, 1993.

[31] *Review of Particle Properties*, Phys. Rev. D **50**, 1180 (1994).

[32] We choose the frequentist approach in order to set our upper limit. See Phys. Rev. **D50**, 1280 (1994).

[33] ARGUS Collaboration, H. Albrecht *et al.*, Phys. Lett. **B199**, 447 (1987).

[34] A. C. Benvenuti *et al.*, Phys. Lett. **B158**, 531 (1985).

[35] T. Liu, *The* $D^0 - \overline{D}^0$ *Mixing Search – Current Status and Future Prospects*, in proceedings of the CHARM2000 Workshop, Fermilab, June 7-9, 1994.

[36] E691 Collaboration, J. C. Anjos *et al.*, Phys. Rev. Lett. **60**, 1239 (1988).

[37] E615 Collaboration, W. C. Louis *et al.*, Phys. Rev. Lett. **56**, 1027 (1986).

[38] CLEO II Collaboration, D. Cinabro *et al.*, Phys. Rev. Lett. **72**, 1406 (1994).

[39] E791 Collaboration, E. M. Aitala *et al.*, submitted to Phys. Rev. **D**, available as hep-ex/9608018 and Fermilab-PUB-96/214-E.

[40] I. Bigi and A. I. Sanda, Phys. Lett. **B171**, 320 (1986).

Appendix A

An Estimate and Parametrization of D^* Mass Resolution

It will be shown in this section that in semileptonic decays, the measured width of the D^* mass peak is limited mainly by the accuracy with which the direction of flight of the D^0 is known, and not so much by the uncertainity in the *magnitude* of the D^0 momentum. A parametrization of the measured D^* width as a function of D^0 decay time will also be obtained.

Since the mixed decays also live longer, the direction of flight of the D for such decays is also better known, resulting in better mass resolution for these decays of interest. Due to this help from nature, the mixing search using semileptonic decays is feasible despite the unobserved neutrino.

The invariant mass of the D^* is:

$$M_{D^*}^2 = E_{D^*}^2 - \mathbf{P}_{D^*}^2 \tag{A.1}$$

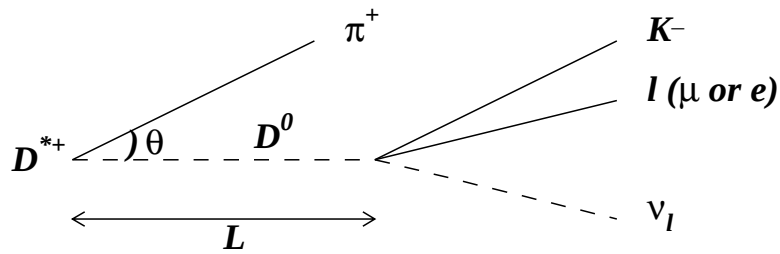

Figure A.1: Schematic of semileptonic decay topology. The measured width of the D^* mass peak is limited mainly by the accuracy with which θ is known.

where E and **P** are the energy and 3-momentum respectively. Now,

$$E_{D^*} = E_{D^0} + E_\pi \tag{A.2}$$

$$\mathbf{P}_{D^*} = \mathbf{P}_{D^0} + \mathbf{P}_\pi \tag{A.3}$$

Using the above expressions for energy and momentum of D^0, and recalling the invariant mass formula $E^2 - \mathbf{P}^2 = M^2$, one gets

$$M_{D^*}^2 = M_{D^0}^2 + M_\pi^2 + 2(E_{D^0}E_\pi - P_{D^0}P_\pi \cos\theta) \tag{A.4}$$

where θ is the angle between the directions of flight of the D^0 and the slow π (see Figure A.1). It follows from the above equation that

$$M_{D^*}\delta M_{D^*} = (E_\pi \delta E_{D^0} + E_{D^0}\delta E_\pi) - (P_\pi \delta P_{D^0} + P_{D^0}\delta P_\pi)\cos\theta + P_{D^0}P_\pi \sin\theta\delta\theta \tag{A.5}$$

Now,

$$E_{D^0} = (M_{D^0}^2 + P_{D^0}^2)^{\frac{1}{2}} \tag{A.6}$$

so that

$$\delta E_{D^0} = \frac{P_{D^0}}{E_{D^0}} \delta P_{D^0} \tag{A.7}$$

similarly,

$$\delta E_{\pi} = \frac{P_{\pi}}{E_{\pi}} \delta P_{\pi} \tag{A.8}$$

Using the above expressions for the errors in the energies of D^0 and π and after some re-arrangement, one gets

$$M_{D^*} \delta M_{D^*} = \sqrt{(a \delta P_{D^0})^2 + (b \delta P_{\pi})^2 + (P_{D^0} P_{\pi} \sin\theta \delta\theta)^2} \tag{A.9}$$

where the errors have been added in quadrature, and:

$$a = \frac{P_{D^0}}{E_{D^0}} E_{\pi} - P_{\pi} \cos\theta \tag{A.10}$$

$$b = \frac{P_{\pi}}{E_{\pi}} E_{D^0} - P_{D^0} \cos\theta \tag{A.11}$$

Now, from data, $P_{D^0} \sim 70$ GeV/c, $P_{\pi} = 6$ GeV/c, $\theta = 10$ mrad. Using these average quantities from data, one gets

$$a = -2.17 \times 10^{-4} \tag{A.12}$$

$$b = 9.54 \times 10^{-}3 \tag{A.13}$$

In the case of completely-constrained hadronic decays, the momentum and hence the direction of flight of D^0 is accurately measured by the magnets. Typical errors in the

magnitude of the momenta are about 1%. The error in angle $\delta\theta$ mainly arises from multiple scattering of the slow π in the target. It can be estimated using the following formula:

$$\delta\theta = \frac{0.014\text{GeV}/c}{P}\sqrt{\frac{X}{X_0}} \tag{A.14}$$

where X_0 is the radiation length for the target, and X is its thickness. E791 uses one platinum target of 0.5 mm thickness and four diamond targets of 1.5 mm thickness each. The above formula yields, for this experiment,

$$\delta\theta = 0.34\frac{0.014\text{GeV}/c}{P} \tag{A.15}$$

For a typical momentum of the slow pion of 6 GeV/c, $\delta\theta = 0.8$ mrad. Using this value for the error in θ, together with equations A.12 and A.13, it follows that

$$M_{D^*}\delta M_{D^*} = \sqrt{(0.00015)^2 + (0.00057)^2 + (0.0034)^2} \quad (\text{GeV})^2/c^4 \tag{A.16}$$

Of the three terms contributing to the D^* mass resolution, note that the last term under the square-root, which arises from angular resolution, is the largest. The other two terms are negligible by comparison.

In the case of semileptonic decays, the momentum of D^0 is not completely measured by the magnets and, as a consequence, the angle θ is also not known accurately. One can estimate the magnitude of the D^0 momentum, and the direction of flight is obtained by measuring the displacement vector between the secondary and primary vertices. Contribution to $\delta\theta$ from the multiple scattering of the slow pion is still the same (about 1 mrad), but the contribution from the measurement error in D^0 direction now dominates. Moreover, the D^* width is a function of decay time of the D^0, since the direction of flight is better known for longer-lived semileptonic decays. In order to demonstrate this, consider equation A.9 again:

$$M_{D^*}\delta M_{D^*} = \sqrt{(a\delta P_{D^0})^2 + (b\delta P_\pi)^2 + (P_{D^0}P_\pi \sin\theta\delta\theta)^2} \tag{A.17}$$

where a and b have been defined earlier, and are independent of decay-time of the D^0. Now $\delta\theta$ can be expressed as:

$$\delta\theta \simeq \frac{\delta r}{l} \tag{A.18}$$

where δr is the quadrature sum of the transverse errors in the positions of the primary and the secondary vertices, and l is the decay length (the separation between the primary and the secondary vertices) of the D^0 . Now,

$$l = \gamma c\tau \tag{A.19}$$

where γ is the relativistic boost and τ is the proper decay time of the D^0 . Now,

$$\gamma \simeq \frac{P_{D^0}}{M_{D^0}c} \tag{A.20}$$

so that

$$\delta\theta \simeq \frac{\delta r M_{D^0}}{P_{D^0}c\tau} \tag{A.21}$$

Thus, equation A.17 can be rewritten as:

$$M_{D^*}\delta M_{D^*} = \sqrt{(a\delta P_{D^0})^2 + (b\delta P_\pi)^2 + (M_{D^0}\frac{P_\pi \sin\theta\delta r}{c\tau})^2} \tag{A.22}$$

In the above equation, first two terms under the square-root sign are independent of the D^0 decay-time, and can be lumped together into one term. Thus, define:

$$\sigma^0 = \frac{1}{M_{D^*}}\sqrt{(a\delta P_{D^0})^2 + (b\delta P_\pi)^2} \tag{A.23}$$

Now equation A.22 can be rewritten as:

$$\sigma = \delta M_{D^*} = \sqrt{(\sigma^0)^2 + (M_{D^0}\frac{P_\pi \sin\theta \delta r}{c\tau M_{D^*}})^2} \tag{A.24}$$

So the the D^* width has two components, one that is constant and another that decreases as the decay-time increases. This was the parametrization used in the likelihood fit.

Equation A.24 can be used to predict the average D^* width. Typically, $\delta r = 12\mu$m , and average decay time is about $\tau = 0.8$ ps in the data. Using average values from data of $\sin\theta \sim 10$mrad, $P_\pi \sim 6$ GeV/c, and $\delta P_{D^0} = 0.15 P_{D^0}$, $P_{D^0} = 70$ GeV/c, one obtains the average D^* width in semileptonic decays:

$$\sigma \sim 3\,\mathrm{MeV}/c^2 \tag{A.25}$$

This predicted estimate of σ is of the same order as the average of σ_L and σ_R (for an average decay time of $t = 0.8ps$) obtained from the fit as listed in table 4.1.

Appendix B

Some Details of Muon Identification

This appendix describes how the number MUCAT, used to classify muon candidates, was calculated, and how the time-to-digital converter (TDC) information was used to predict the X position of a hit in the Y wall.

B.1 Calculation of MUCAT

MUCAT is a number that describes the goodness of a muon tag. The higher the number, the better the tag. The value of MUCAT is determined according to Table B.1 below.

B.2 Use of TDC Information in Y Muon Wall

The TDC information was used to predict the X position of a hit on the Y wall for the tracks that had no corresponding hit in the X wall. The X-wall paddles were too noisy for the X-TDC information to be useful, so that only Y-TDC information was used in this analysis.

MUCAT	Tagging Requirements
10	Projected X paddle AND projected Y paddle are hit.
9	Projected Y paddle is hit, AND there is a hit in the X wall within 1.64σ of the projected X position.
8	There is a hit in the Y wall within 1.64σ of the projected Y position AND the projected X paddle is hit.
7	There is a hit in the Y wall within 1.64σ of the projected Y position AND a hit in the X wall within 1.64σ of the projected X position.
6	Projected Y paddle is hit AND there is NO hit in the X wall within 1.64σ of projected X position.
5	There is NO hit in the Y wall within 1.64σ of projected Y position AND the projected X paddle is hit.
4	There is a hit in the Y wall within 1.64σ of the projected Y position AND there is NO hit in the X wall within 1.64σ of projected Y position.
0	NONE of the above is satisfied.

Table B.1: Description of the tagging requirements of a muon candidate for a given value of MUCAT

In order to derive the relation between the X-position of the hit on the Y wall and TDC counts, a scatter plot of Y-wall TDC counts vs. projected X-position of the hit was plotted for the data muon candidates that had MUCAT = 10, where MUCAT has been described in the previous section. These are muon candidates with coincident hits in both X and Y walls and are thus likely to be 'good' muons. Figure B.1(a) shows the scatter plot of TDC counts vs. projected X position of the track for such muon candidates. A clear correlation is seen between the projected X position and TDC counts. Figure B.1(b) shows a similar scatter plot for the muon candidates that had MUCAT ≤ 4. These correspond to 'lower' quality muons, and no correlation is visible between the projected X position and the TDC counts. These muon candidates could come from decays in flight (in which case projected X position based on track parameters won't match the actual hit position) or punch-through particles. The difference between these two plots suggests that TDC information can be used to obtain a cleaner sample of muons.

Figure B.1(a) was used to obtain a relationship between the projected X-position of a track on the Y wall and the corresponding TDC count. The equation obtained was:

$$X \text{ (cm)} = -10.53 * TDC + 1929.65 \tag{B.1}$$

Only a small subsample (less than 2%) of the real data was used to obtain the above equation, so that the analysis is not biased when this equation is used to predict the X-position of a track based on TDC information.

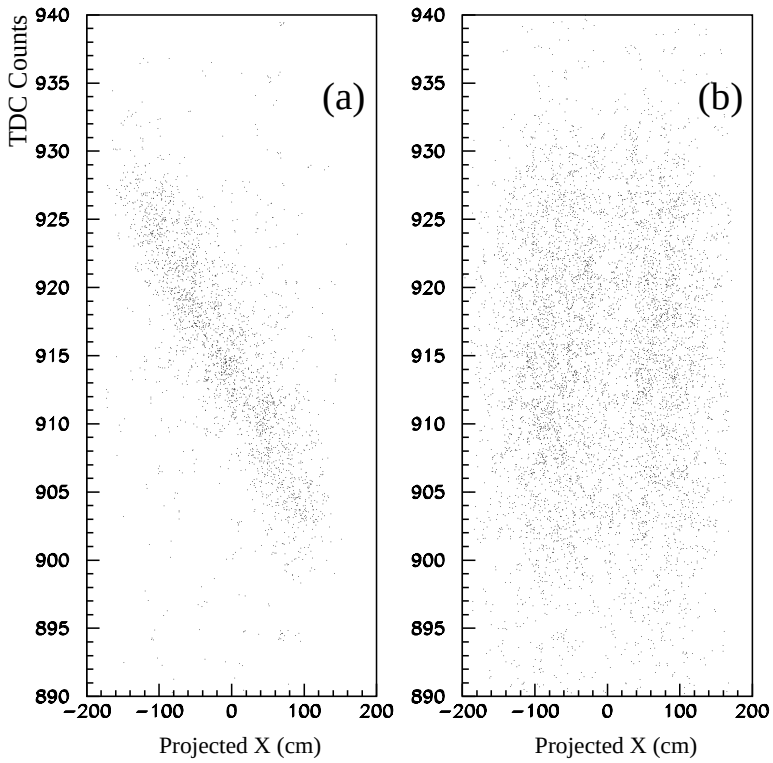

Figure B.1: Scatter plots of Y-wall TDC counts vs. projected X-positions of tracks on the Y muon wall. Figure (a) is for the tracks that have MUCAT = 10, i.e., the tracks that have hits associated with them in expected scintillating paddles in both the X and the Y wall, implying that these are 'good' muons. Figure (b) is for the tracks that have MUCAT ≤ 4. These are 'not good' muons. A clear correlation is seen between the TDC count and projected X position for good muons in Figure (a). In Figure (b), no clear correlation is visible. This correlation between TDC count and projected X position on the Y muon wall was used to obtain a relationship between the Y TDC counts and the X positions of the hit.